Effect of chordwise flexibility and depth of submergence on an oscillating plate underwater propulsion system

by

Oleksandr Barannyk
B.Sc. in Mathematics and Computer Sciences, Poltava State University, 2001
M.Sc. in Applied Mathematics, New Jersey Institute of Technology, 2003

A Thesis Submitted in Partial Fulfillment of the
Requirements for the Degree of

Master of Applied Sciences

in the Department of Mechanical Engineering

University of Victoria

Effect of chordwise flexibility and depth of submergence on an oscillating plate underwater propulsion system

by

Oleksandr Barannyk
B.Sc. in Mathematics and Computer Sciences, Poltava State University, 2001
M.Sc. in Applied Mathematics, New Jersey Institute of Technology, 2003

Supervisory Committee

Dr. Brad Buckham, Co-Supervisor
(Department of Mechanical Engineering)

Dr. Peter Oshkai, Co-Supervisor
(Department of Mechanical Engineering)

Dr. Curran A. Crawford, Departmental Member
(Department of Mechanical Engineering)

Dr. Marcelo Laca, Outside Member, Uvic Non-unit Member
(Department of Mathematics and Statistics)

Supervisory Committee

Dr. Brad Buckham, Co-Supervisor
(Department of Mechanical Engineering)

Dr. Peter Oshkai, Co-Supervisor
(Department of Mechanical Engineering)

Dr. Curran A. Crawford, Departmental Member
(Department of Mechanical Engineering)

Dr. Marcelo Laca, Outside Member, Uvic Non-unit Member
(Department of Mathematics and Statistics)

ABSTRACT

The first part of this work was dedicated to the experimental study of basic principles of oscillating plate propulsors undergoing a combination of heave translation and pitch rotation. The oscillation kinematics are inspired by swimming mechanisms employed by fish and some other marine animals. The primary attention was the propulsive characteristics of such oscillating plates, which was studied by means of direct force measurements in the thrust-producing regime.

Experiments were performed at constant Reynolds number and heave amplitude. By varying the Strouhal number, experimental depth and chordwise flexibility of the plate it was possible to investigate corresponding changes in thrust and hydromechanical efficiency. After numerous measurements it was possible to establish an optimal set of parameters, including the system's driving frequency, the ratio of rigid to flexible segment length of the plate and the range of Strouhal number, that led to a peak efficiency near 80%.

The experiments for different values of chordwise flexibility showed that greater flexibility increases the propulsive efficiency and thrust compared with similar motion of the purely rigid foil. By submerging the plate at different depths, it was observed that the proximity of the propulsor to the channel floor led to overall increase in the thrust coefficient. However the increase in thrust coefficient was pronounced in the range from middepth to the floor of the water tunnel. The special case when the upper plate's edge is tangential to the undisturbed free surface is discussed separately.

The second part of this work introduces a semianalytic approach for calculating the influence of piezoelectric (PZT) actuators on the free vibration characteristics of an Euler-Bernoulli clamped free beam. The beam represents a simplified version of the fish tail whose stiffness is proposed to be controlled by placing a pair of PZT actuators in strategic regions along the caudal area of the tail. This approach, according to earlier studies, improves efficiency if tail natural frequency matches tailbeat frequency.

The approach used an existing form of a transfer matrix technique developed for the analysis of non-proportionally damped slender beams. The PZT dynamics were incorporated into this recursive procedure through a modification that accounted for the tendency of the PZT patches to couple the dynamics of the node points of the segmented Euler-Bernoulli beam. To ensure stability of the system, an angular velocity feedback law, originally motivated by vibration suppression applications, was chosen for the PZT actuators. The sensitivities of the tail modes of vibration to the location of the PZT elements and the control gain were determined. Mode shapes for the revised modes were determined and it was shown that the first, second and the third modes maintained similar norms as tail shapes observed in *anguilliform*, *subcarangiform*, and *thunniform* regimes of swimming. Using a semianalytic approach, it was shown that PZT location heavily influences the frequency distribution of the modes of vibration. The control gain, when chosen within the limit of saturation voltage, is shown to be an effective control lever for vibration suppression and at rising the tail stiffness during rapid acceleration when the fish accelerates. However, the single PZT patch does not provide significant frequency adjustments such that different swimming modes could be employed efficiently with a single mechanical tail system primary actuator. To pursue such versatility for the fish tail, the tail structure must be very flexible to accommodate the significant frequency increase caused by the addition of the PZT material. Also, the use of additional PZT patches and negative control gains must be considered in order to use the PZT's to drop the higher modes (second and third) down into the frequency range of the primary actuation system, presuming the tail and primary actuator are designed for a *thunniform* regime of swimming.

Contents

List of Tables

List of Figures

ACKNOWLEDGEMENTS

My deepest gratitude goes to my wife Vasylyna and my son Dimitri, as well as my dad, my mom, and my sister Lyudmyla, who have always been supportive throughout my entire graduate study. Completion of this thesis was simply impossible without them.

I would like to extend my thanks to the people that were directly involved with the development of this work, my supervisors Dr.Brad Buckham and Dr.Peter Oshkai, whose encouragement, guidance and support from the initial to the final level enabled me to develop an understanding and appreciation of the subject. Dr.Buckham and Dr. Oshkai were always accessible and willing to help their students with their research. As a result, research life became smooth and rewarding for me.

My thanks are also directed towards the people who provided help and advice with the practical aspects of my laboratory projects, especially Patrick Chang, Rodney Katz, , Dr.Curran Crawford, Brian Sennello (Motion Control Systems, North America), Steven Anderson (LaVision Inc.).

Finally, I would like to thank all the friends who turned these graduate years into a very pleasant experience.

DEDICATION

This thesis is dedicated to my father, Leonid Barannyk, a brilliant mathematician, who taught me that the best kind of knowledge to have is that which is learned for its own sake.

Chapter 1

Introduction

1.1 Biomimetic propulsion

For centuries, aquatic species have developed highly efficient swimming mechanics that are individually optimized to their specific natural habitant. Inspired by observations of fish and marine mammals, scientists and engineers have invented vehicles whose operating principles attempt to mimic swimming kinematics. The ability of various species to achieve high velocities, rapidly change direction or to hover at a spot in moving water, are very desirable for autonomous underwater vehicles (AUVs). AUV applications in security, science and remote monitoring require the high efficiency, stability and manoeuvrability believed possible if biomimetic propulsion can be employed.

It is common knowledge that fish achieve propulsion by using their muscles to oscillate their tails. However, some muscles are not directly responsible for the gross tail locomotion, but rather to modulate the effective stiffness of the tail. This was shown by Long [1], after series of experiments on a largemouth bass. These muscles actively change the mechanical property of the fish's tail in response to the changes in the regime of operation (i.e. cruising speed) or changes in the surrounding environment(i.e. current magnitude or direction).

Long [1] proposed that fish minimize the mechanical cost of bending by modulating their body flexural stiffness, effectively tuning their body's natural frequency to match the tailbeat frequency at current swimming speed. This theory is supported by several experimental studies. While it does not modulate the stiffness of its bell actively in this manner, the jellyfish appears to swim at a cycle frequency at or near the resonant frequency of its bell, thus maximizing the bell's deformation and thrust with minimal input of energy [2]. Swimming scallops also swim at or near the resonant frequency of their deforming propulsive structures [3].

The swimming speed of a fish is often measured in body length per second (BL/s) [4], and it is interesting when this metric is used to compare fish to current state of the art machines that employ conventional types of propulsion. For instance, as summarized in Figure 1.1, dolphins and the fastest fish can travel through water at up to 8 BL/s. A small bird, such as the Starling, is capable of reaching 120 BL/s. On the other hand, a Boeing 747 at its top speed can only achieve 3.8 BL/s. Even fighter jets such as RAF Tornado, which can reach 38 BL/s, is still far from the Starling's standards. Even more impressive is the Desert Locust, a tiny insect, whose top speed is an amazing 180 BL/s.

Figure 1.1: (a) Dolphin: 8 BL/s, (b) Starling: 120 BL/s (c) Desert locust: 180 BL/s (d) Boeing 747: 3.8 BL/s (Boeing ©) (e) RAF Tornado: 38 BL/s (Taken from www.hickerphoto.com, www.raf.mod.uk)

The interest in flapping-wing, or oscillating foil devices from an engineering point of view is due to their performance and energy and material efficiencies. For aquatic vehicles, these type of propulsors are more ecologically friendly than common propeller type propulsors [5]. Aquatic apparatus that are used for underwater exploration, accident investigations and biological data gathering, often operate in sensitive areas with considerable biodiversity, and it is important to avoid significant alteration of the local habitat. Due to the fact that an oscillating foil system operates at relatively low frequency, marine vessels equipped with these propulsors are not dangerous to surrounding aquatic life, be that fish, animals or coral riffs.

Another benefit of oscillating foil propulsors is that they are capable of operating in different regimes of motion. By employing steady periodic swimming, characterized by cyclic repetition of propulsive movements, it is possible to cover relatively large distances at a relatively constant speed [4]. On the other hand, oscillating foil propulsors are also capable of transient movements that include acceleration, escape maneuvers and sharp turns – very rapid types of motion. Finally, oscillating foils used in combination with a control device and a stabilizer can accomplish station keeping, or hovering, in the presence of significant hydrodynamic disturbances. This is especially appealing for military or scientific underwater research applications that require extended observations at one location in the ocean.

1.2 Oscillating foil technologies

Oscillating foil propulsors have already been shown to generate thrust efficiently. Japanese scientists [6] along with the company, Hitachi Tsozan in Osaka, investigated propulsion of a large surface vehicle with an oscillating foil propulsion device. In 1984, they developed plans for two ships, of lengths 27 m and 300 m respectively, each equipped with thruster-wings for capturing the energy of waves. According to the company Hitachi Tsozan, a 300-meter ship can accelerate up to 11 knots with just the energy supplied by the oscillating wings extracting energy from waves, and no engine assistance. When moving into port in the absence of heavy seas, or when an increase of speed is required beyond that supplied by wave energy, power from the ships engines will be applied to oscillate the wing more rapidly. In [6], it was found that for some regimes of oscillation it was possible to reach efficiency as high as that of a screw propeller for the same expended power. The experiments in [6] also showed that oscillating foil propulsors can be as effective as propellers while creating less noise and vibration in the vehicle.

Considering the other benefits of the oscillatory thruster, it was seen to be advantageous over a traditional screw-type thruster. Consider the following special features of an oscillatory thruster: the extraction of wave energy occurs irrespective of the direction of movement of waves and wind, including counter movement of a ship; in contrast to a sail, the propulsor does not occupy space on the deck; the oscillating foils beneath the ship also serve as stabilizers.

Following Long's observations [1] on the benefits of flexibility in the foil and/or the foil driving mechanism, Harper et al. [7] proposed a model that uses springs to transmit forces and moments from actuators to the tail to create an oscillatory motion. This was motivated by biomechanists assertions that fish tendons may store energy like springs when transmitting forces from muscles. It was shown that the energy cost for heaving motions of a hydrofoil oscillating at 0.19Hz can be reduced by up to 33% when the hydrofoil support structure stiffness is properly tuned through an optimal choice of spring stiffness.

With current state of the art mechatronics technologies, new possibilities exist for constructing a robotic fish that mimics the motion of a real fish. Flapping-foil propulsors can now benefit from use of modern microcontrollers and actuators such as MEMS, piezoelectric devices, reciprocating chemical muscles, etc. In particular, reciprocating chemical muscles are capable of generating autonomic foil oscillation from a chemical energy source, and hence can be used as a drive mechanism for the oscillating foils. Among the most convincing of animatronics fish are the artificial sea bream and coelacanth developed by Mitsubishi Heavy Industry in Japan, shown in Figure 1.2 [8].

Figure 1.2: Robot-Coelacanth, Mitsubishi Heavy Industry, Japan

The work of [9],[10] deals with experimental observation of pectoral fin motions of a Black Bass. A remotely operated vehicle (ROV) controlled by a computer was developed to mimic the observed fin motion of Black Bass. The vehicle, shown in Figure 1.3, was used to study the role of pectoral fins in improving the maneuverability of ROVs.

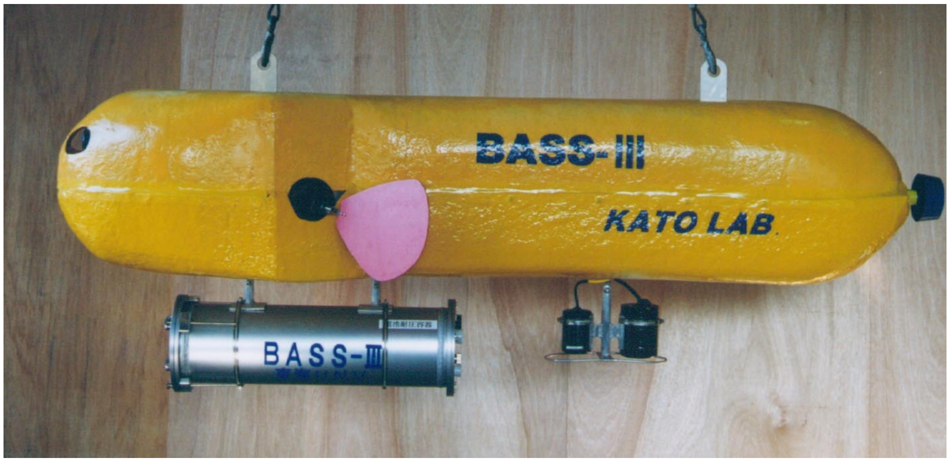

Figure 1.3: "BASS-III" Kato lab, Japan. Pectoral fins are used both for propulsion and steering. (courtesy of Dr. N. Kato)

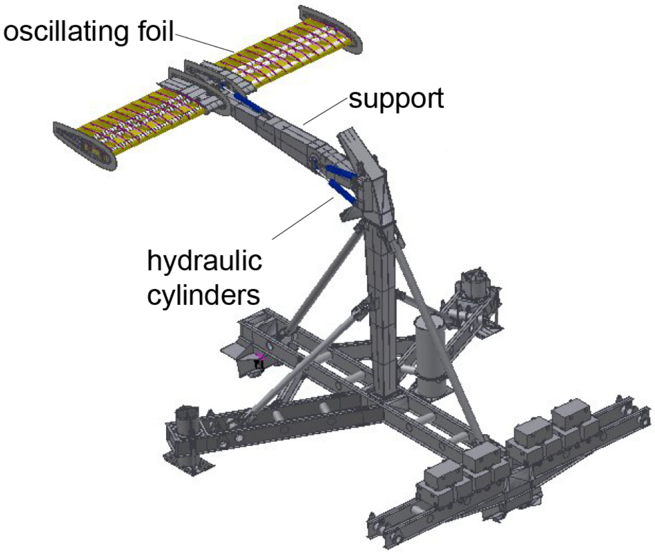

Figure 1.4: "Stingray" tidal energy device. (courtesy of IHC Engineering Business Ltd)

The hydrodynamic characteristics of oscillating foils have also been exploited outside of the fish swimming paradigm. The Stingray device shown in Figure 1.4 is used to capture energy from underwater currents. The main difference between optimization for the Stingray device and that for a propulsor is whether the foil generates thrust or drag. Thrust generation corresponds to locomotion, drag corresponds to power capture. Only a few oscillating foil systems, such as Stingray exist, and these devices rely on an optimal pitch angle schedule of the foil to drive oscillation of the support arm which causes a stroke of the hydraulic cylinders. In 1997, the "Engineering Business" set up the Stingray program to develop a device, shown in Figure 1.4, that employed the oscillating foil principle for energy capture. The prototype was tested off the Shetland Isles in 2002 and 2003, and showed reasonably good results; it was able to generate 122kW with flow speed of 2.2m/s and demonstrated acceptable results at lower current speeds. Unfortunately, the device was shelved shortly due to financial constrains.

1.3 Force measurement for oscillating foil propulsion

Regardless of the application, the characterization of the lift and drag forces acting on an oscillating foil is vital to the design of an oscillating foil system. Force measurement techniques used in flapping-wing propulsion experiments can be classified into direct experimental force measurement and force measurements by vorticity fields.

Sunada in [11] studied unsteady fluid dynamic forces acting on a two-dimensional wing in sinusoidal heaving and pitching motion. In that work, unsteady fluid dynamic forces were measured directly by a load cell. By using the measured fluid dynamic forces, authors identified combinations of plunging and pitching motions for maximum time-averaged thrust and for maximum efficiency.

Another example of a direct force measurement technique is presented in the work by Read at al. [12], where the experimental study of the propulsion is performed on a heaving and pitching hydrofoil, with measurement of lift and thrust forces. The article presents conditions of high performance under significant thrust production and a series of tests on a flapping foil that produced forces needed for maneuvering of an apparatus equipped with such form of propulsor.

A well known method for measuring forces exerted by a fluid on a bluff body from the flow-field quantities is Lighthill's so-called impulse concept [13], [14]. This technique allows one to determine instantaneous force in terms of the time-rate of change of the momentum of the distributed vorticity about a body in the fluid. The central part of this approach is the statement that the force on a body may be divided into (i) potential flow force that depends linearly on the body velocity and can be accurately calculated; and (ii) a vortex-flow force that varies nonlinearly and is related, definitively, to vortex shedding and to convection of shed vorticity.

Advancements in flow visualization make the idea of calculating force exerted by the fluid on the bluff body from the measured flow-field quantities very attractive. In particle image velocimetry (PIV) the fluid motion is made visible by introducing small tracer particles into the flow. From positions of these tracer particles at two instances of time, i.e. the particle displacement, it is possible to reconstruct the flow velocity field. In [15], the PIV technique was combined with Lighthill's impulse concept in an experimental study on the distribution of vorticity clusters about a sinusoidally oscillating cylindrical body in quiescent fluid. In [15] it was noted that the shed vorticity concentrations in the immediate proximity to the body have consequence on the lift coefficient only if they have departed the cylinder's vicinity. It is therefore necessary that all of the vorticity generated from the cylinder remains within the field of view of the PIV imaging system, and this presents a challenge to the execution of the PIV technique.

The theoretical concept introduced by Lighthill was extended in [16] to take into account the fact that all of the previously generated vorticity may not be within the field of view of a PIV imaging system. This approach introduces a control volume concept and involves elimination of the pressure term. The clear advantage, and a primary motivation of the vorticity-based approaches, is that a direct relationship between the space-time development of the vorticity field and the body loading is clearly evident, even though the accurate calculation of the vorticity downstream of the body is still not fully completed. Results presented in the work of Noca in [16] assess various control volume representations. Noca compared the consequence of location of the control volume boundaries and position vectors relative to the flow pattern determined by PIV. Within this work a so-called flux equation was formulated to yield time-dependent forces from PIV data acquired only on a finite domain surrounding the entire body.

Recently, more advanced mathematical tools have found their application in force estimation from wake measurements. The paper of Dabiri [17] addressed the question of what minimal set of wake properties is sufficient to determine hydrodynamic forces. It was demonstrated that the velocity-pressure perspective is equivalent to the vorticity-added-mass approach in the equation of the motion. Dabiri developed a mathematical model to approximate the contribution of wake vortex added-mass to locomotive forces, given a contribution of velocity and vorticity field measurements in the wake. By tracking the motion of individual fluid particles in the flow (the Lagrangian perspective) instead of analyzing the entire velocity field at each instant of time (the Eulerian perspective), it was possible to quantitatively determine the boundaries of vortices in a measured flow without changing the frame of reference of the measurements. The forces generated by a body submerged into a fluid at a constant motion, contain contribution from wake vortex added-mass. Given the wake vortex boundaries, the added-mass of the wake vortices must be measured to determine the magnitude of the wake vortex added-mass contribution. This method, however, has its limitations which is symmetric vortex ring wakes such as those generated by jellyfish, squids and slaps, and can not be used to elucidate the structure of more complex wakes.

1.4 The effect of chordwise flexibility and depth of submergence

There are several theoretical and experimental investigations of elasticity effects on flapping-wing propulsor. Katz in [18] found that increasing the flexibility of a foil undergoing large amplitude oscillatory motion increased the propulsive efficiency by 20%. However, compared to a similar motion of a rigid foil, a small decrease in overall thrust was observed. These conclusions were made based on uniform chordwise flexibility and mass distribution.

Young in [19] analyzed the influence of locust wing elastic deformation on its aerodynamic characteristics. A three-dimensional computational fluid dynamics (CFD) simulation based on wing kinematics was used for that purpose. The results were validated against smoke visualizations and digital particle image velocimetry completed for real locusts. It was shown that wing deformation in locusts is important both in enhancing the efficiency of momentum transfer to the wake and in directing the aerodynamic force vector appropriately for flight.

Tatsuro in [20], [21] investigated the propulsion of a partially elastic foil and concluded that such a foil can achieve higher efficiency for a given thrust than a rigid one, and that the chordwise mass distribution and stiffness characteristics have a significant effect upon the propulsive characteristics. These conclusions were made by applying a linear theory for the foil elasticity.

The effect of surface proximity on the performance of a oscillating foil propulsor was studied in the theoretical work of [22]. It was found that the energy wasted to generated surface waves is a dominant part of efficiency drop, and that increasing submergence leads to an increase in thrust. Similar observations were reported in [23]. It was noticed that the influence of free surface waves is different for foils of different aspect ratios. A foil with a small aspect ratio generate larger free surface effects than those created by a foil with a larger aspect ratio. Henceforth, the reduction of thrust and efficiency due to induced drug is much stronger for foils with small aspect ratios.

1.5 Mechanical stiffness control and its application in biomimetic propulsion

In addition to using a flexible support structure to improve the efficiency of oscillating propulsors, active structural control could be achieved by means of piezoelectric transducer (PZT) actuators bonded to strategic locations of the tail surface. The technique would exploit the tendency of the piezoelectric strips to extend or contract, when subjected to a voltage. The deformation induces a shear force on the surface of the hydrofoil that can oppose or accentuate the structural deformation. One of the benefits of employing piezoelectric actuators is that PZT patch voltage can be set proportional to the deformation of the foil, and thus the PZT patches can drastically alter the natural modes of vibration of the foil. Depending of the fish swimming regime [24], which is illustrated in Figure 1.5, the flexible foil could be representative of a single caudal fin as in Figure 1.5(d) or the whole fish body as in Figure 1.5(a), or the tail section in Figure 1.5(b), (c) or (d).

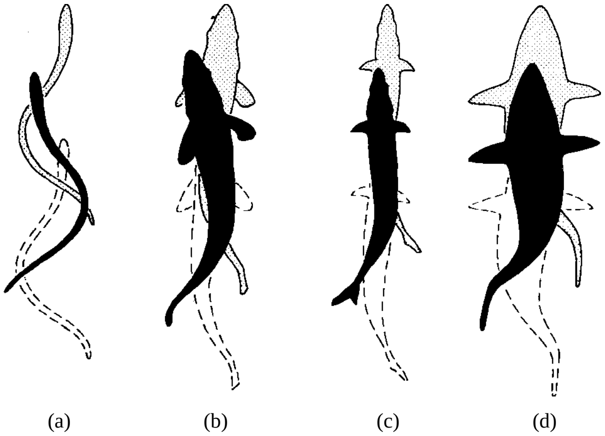

Figure 1.5: Gradation of fish swimming movements (a) anguilliform, (b) subcarangiform (c) carangiform (d) thunniform. (Taken from Lindsey [24])

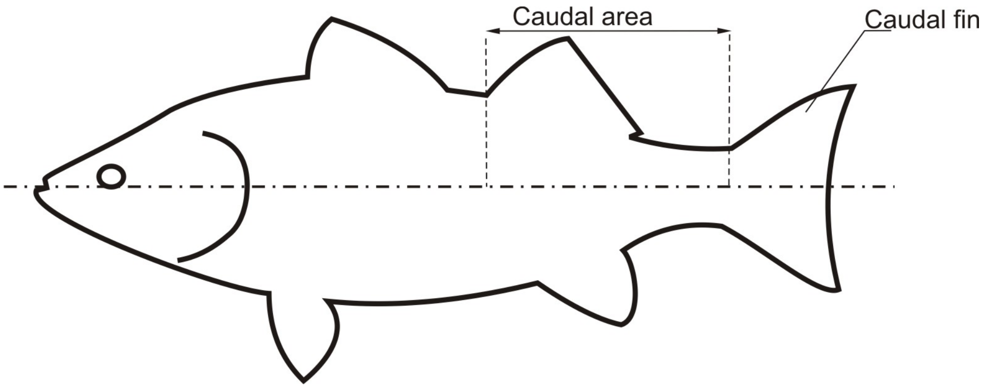

Figure 1.6: Most fish generate thrust by bending their bodies into backward-moving propulsive waves that traverse the caudal area to the caudal fin. This is referred to as body and/or caudal Fin (BCF) locomotion.

Fish swimming is very complicated process, most of the fish achieve propulsion by using their muscles to oscillate their tails. As the major portion of thrust is coming from the fish tail, that consists of caudal area and caudal fin, illustrated in Figure 1.6, it is natural to consider this part of the fish as a model for an alternative form of mechanical propulsion. Since the fish tail motion is accomplished via an interaction between the caudal area and caudal fin. This thesis consist of two main parts, each dedicated to a particular section of the fish tail. The first part deals with the experimental investigation of what caudal fin kinematics and mechanics are ideal. The second part is dedicated to the caudal area of the fish tail, which is studied in the content of how PZT actuators could be used to assist the tail oscillations that generate the ideal fin kinematics.

The motivation for using PZT actuators shows from two observations: (i) that tail natural frequency ideally matches tailbeat frequency, (ii) that surface bonded PZT's have been applied to alter natural vibration of slender structures. The major considerations in using PZT actuators to control flexibility of a slender structure are as follows:

(1) the choice of feedback law for the PZTs.

(2) the choice of location and the control gains of the PZTs.

1.5.1 The Piezoelectric Effect

The piezoelectric effects depend on the state feedback law used to synthesize the PZT control voltage. When subject to a control voltage, the piezoelectric material tends to extend or contract depending on the polarity of the voltage. If the voltage can be set proportional to the deformation of the beam surface, the PZT can create a shear force on the beam surface that either diminishes or exacerbates the beam deformation.

Sun at al. [25] utilized an L-type linear velocity feedback control to command voltage applied to PZT actuators. The choice was dictated by the ease of obtaining linear velocity data through integration of acceleration, measured by small accelerometers mounted on the beam, or differentiating deformation measured by position-sensitive detector. The use of linear velocity feedback comes with a cost, as actuator placement needs to be performed very accurately to avoid instabilities. The authors in [25] proposed three conditions in order to ensure stability. To start, actuators were positioned in the region where the eigenfunction and its first spatial derivative, had uniform sign over the length of the actuator. Secondly, actuators should be placed to avoid inflection points, where the second derivative of the eigenfunction changes its sign. Finally, actuators were placed in regions with the maximum vibration damping effect. L-type control, even with constraints mentioned above showed promise in suppressing vibration.

Alternative to L-type control is a control strategy based on angular velocity feedback, or simply A-type control. Gurses at al. [26] extended previous work by Sun et al.[25] in applying A-type control strategy. The advantage of A-type control is that it is unconditionally stable, but it is technically challenging to obtain angular velocity data. From theoretical and experimental investigation of a novel fiber optic shape sensor, ShapeTape$^{\text{TM}}$ from Measurand Inc., authors were able to obtain both angular and linear velocity feedback and to realize composite PZT actuator control scheme that combined the L-type and A-type PZT control laws. As they are both proportional to the time rate of change of the beam deformation, the L and A-type methods appear as non proportional viscous effects in the motion equations.

Classically, the partial differential equations of motion governing the free and undamped vibration of distributed parameter systems, such as strings, rods, shafts and beams are solved using a standard separation of variables technique. With no system damping (external or within the structure), these solutions yield strictly real-valued normal modes and natural frequencies. Addition of viscous damping effects, that are uniformly distributed throughout the system also produces a simple solution, but a viscous damping distribution which is not constant across the spatial domain is generally not proportional to a linear combination of the inertia and stiffness at all locations. Hence, one or more non-linear, complex-valued, transcendental equations must be simultaneously solved for the natural frequencies.

In many existing analysis of non-proportional systems, approximate proportional damping distributions are introduced, or simplified system configurations are considered with lumped damping at boundary locations. However, for certain non-proportionally damped problems, Laplace's transform [27] or integral equations [28] provide very good solutions to the complex modes without such approximation.

In [29], the transfer matrix method is used to solve the equation of free vibration of nonproportionally damped slender beams. The governing differential equation was written in first order form in terms of displacement, slope, bending moment and shear. The method in [29] subdivides the slender structure by adding node points at the locations of any lumped damping or stiffness elements and/or discontinuities in the internal stiffness and damping, thus allowing the structure of any complexity to be considered. The transfer matrix method can also be adopted to structures with rather complicated internal boundary conditions and damping models as was shown in Sorrentino et. al [30]. Assuming a beam to be a concatenation of homogeneous segments, the authors transformed the global boundary value problem to a system of first order ODEs for each segment, each of which could be solved by applying appropriate boundary conditions on displacement, slope, or internal shear or bending moment. The transfer matrix technique was applied to enforce specific discontinuities in shear and bending moment between sections of the beam. The approach generated a recursive series of equations from which one can extract the eigenvalues and express the eigenfunctions in analytical form.

1.5.2 Designing Smart Structures

The proper placement and gain selection of the PZT patches is a challenging problem in the design of actively damped structures. Crawley in [31] was the first to give a practical solution for placement strategy. His approach was to place PZT actuators, which locally strain the beam to which they are attached, in the regions of high average strain and away from areas of zero strain. In order to find these "strain nodes", one should differentiate the analytic expressions for the beam modes and find zero-crossing points of resulting functions. However the placement problem for the case of two or more controlled modes was not addressed. In addition Crawley emphasized the use of segmented actuators for control of flexible structures, since the ability to independently adjust the voltage applied to each PZT provides more effective control of the flexural modes.

Sadri at al. in [32] presented a technique for the optimal placement of PZT actuators on the cantilever plate structure using modal controllability. The algorithm works on calculation of the gross degree of controllability for all possible combinations of actuator locations. By applying an advanced automated search routine, the actuator location at which the degree of controllability was maximized was obtained.

In the paper by Santosh et al. [33], the approach to simultaneous placement and sizing of PZT actuators was presented. The strategy was formulated as an optimization problem. In the passive damping case, the authors measured the system performance for a particular choice of controller, placement and piezo length by rate of decay of system states and therefore sought to place the poles of the system far into the left half of the complex plane. Linear quadratic regulatory method was the second optimization procedure applied by Santosh et al. The advantage of that method was that the optimizing performance was insensitive to initial conditions.

Moheimani and Ryall in [34] addressed the problem of choosing the optimal location for PZT placement via the notion of modal and spatial controllabilities. The modal controllability is a measure of controller authority over each mode. When it is zero the controller has no authority over that particular mode, if the mode has 100% of modal controllability, the controller has maximum authority over that mode. Similarly, the spatial controllability can be defined as the controller authority over the entire structure in an averaged sense. The major statement of [34] is that it is possible to form a constrained optimization problem, where the spatial controllability of the structure is maximized, while insuring that the modal controllability of the dominant modes is above a desired threshold.

Sorrentino et. al [30] confirmed that an optimum external damping distribution may be chosen to control particular modes, and also showed that increasing the level of damping via PZT actuators does not yield predictable effects in the natural modes of vibration. In [30], it is mentioned that various damping laws can be used simply by modifying the state dependent definition of the damping function. However, to the author's best knowledge, only those lumped damping elements that depend on the local state can be incorporated using the methodology of [30]. For the case of the actively controlled PZT patches, the moments and forces developed at the boundary of the patch depend of the state of the beam deformation at both node points, and incorporation of PZT dynamics into the methodology of [30] requires significant revision to the technique.

1.6 Objectives

The main goal of this research is to establish the range of parameters for the optimal performance of an oscillating flexible plate propulsion system. This propulsion system represents the caudal area of the fish linked to a caudal fin, as shown in Figure 1.6, and a study of each of these parts is required.

The caudal fin can be approximated by an oscillating flexible plate. The first part of the thesis is aimed at establishing the sensitivity of an oscillating flexible plate's propulsive performance to the chordwise flexibility and depth of submergence. This goal will be achieved through a series of experiments that involve direct force measurements on a plate of several rigidity types, operating in different experimental depths. The secondary objective of this thesis is to investigate a means of ensuring an optimal relationship between the changing tailbeat frequency and the flexibility of the caudal area of the tail that generates the fin oscillations. It is planned to develop a method for quantifying the effect of PZT's on the tail's natural modes of vibrations, such that PZT placements and gains can be identified for future oscillatory foil propulsors. The expected contributions of this thesis can be listed as follows.

(1) Through the direct force measurements on a periodically oscillating plate, submerged in the middepth of the test section of the water channel, it will be established what types of plate produce greater thrust and efficiency.

(2) The sensitivity of the oscillating propulsion system to variation in the system driving frequency, heave amplitude and plate geometry will be determined. The set of parameters for an optimal performance will be identified.

(3) The dependance of the propulsive characteristics of the plate on proximity to a free surface will be investigated by performing series of experiments for five experimental depths

(4) The modified transfer matrix technique of [30] will be applied to incorporate the effects of piezoelectric actuators that are perfectly bonded to a flexible structural element. For this work, the flexible element is represented by an Euler-Bernoulli beam model of the caudal area or tail.

(5) The sensitivity of the caudal tail frequencies and mode shapes to the PZT position and control will be established using the revised transfer matrix technique.

1.7 Thesis Overview

In Chapter 2 the detailed problem overview is presented. The flow facility, experimental apparatus and the range of parameters studied are discussed in order to provide the reader with good understanding of how the force measurements are conducted. The experimental procedure is introduced along with applicable hardware setup and software pre- and postprocessing. The accuracy of equipment used and the overall error in the measurements are discussed.

In Chapter 3 contains the major experimental part of this work. Here, the oscillating plate propulsion system's performance is investigated, while submerged in the middepth of the water channel test section. A comparison study was performed, it first determines the optimal driving frequency for high efficiency and thrust. Second, that frequency is used to determine the optimal heave amplitude. Third, changes in the ratio of the flexible and rigid sections of the plate are investigated. This comparison study strives to find the set of parameters that produce to the highest efficiency and thrust from the oscillating plate propulsion system. The last part of this chapter deals with the effect of depth of submergence and its influence of the performance of the oscillating plate propulsion system along with the illustration of flow patterns.

In Chapter 4 the semianalytic approach for calculating the influence of piezoelectric (PZT) actuators on the free vibration characteristics of an Euler-Bernoulli clamped-free beam is introduced. The Euler-Bernoulli beam model approximates the propulsion element represented by either the caudal area or the tail. The stiffness control of the flexible tail is imposed through the recursive procedure that accounts for the tendency of the PZT patches to couple the dynamics of the node points of the segmented Euler-Bernoulli beam. To ensure stability of the system, an angular velocity feedback law, presented in existing work on vibration suppression, was chosen for the PZT actuators. The sensitivities of the modes of vibration to the location of the PZT elements and the control gain are determined.

Chapter 5 presents the methodology for defining the optimal locations for the PZT actuators, along with the discussion of PZT effect on frequencies and mode shapes. The comments on potential applicability of the proposed technique to the design of biologically inspired propulsion systems are presented at the end of this chapter.

Finally, in Chapter 6 the conclusions and contributions of this thesis are summarized and the recommendation for the future research are presented.

Chapter 2

Experimental system and technique

2.1 Flow facility

Experiments were conducted in the flow visualization water tunnel in the Fluid Mechanics Laboratory of the Department of Mechanical Engineering at the University of Victoria.

Historically, water tunnels have been utilized in one form or another to explore fluid mechanics and aerodynamic phenomena since the days of Leonardo da Vinci. They have been recognized as highly useful facilities for critical evaluation of complex flow fields associated with many modern vehicles such as high performance aircrafts.

In particular, water tunnels have filled a unique role as research facilities for understanding the complex flows dominated by vortices and vortex interactions. Flow visualization in water tunnels provides an excellent means for detailed observation of the flow in a wide variety of configurations. The free stream flow and the flow field dynamics in a water tunnel are characterized by relatively low speed, allowing real time visual assessment of the flow patterns using a number of techniques, including injection of dye flow through ports in the model, hydrogen bubble generation from strategic locations on the model, or laser light sheet illumination of flow tracers.

The water tunnel, Figure 2.1, that was employed in the current investigation was of a re-circulating type, with the closed flow loop arranged in a vertical configuration. The components of the tunnel included a test section, filtering station and a circulating pump with a variable speed drive assembly. The water tunnel had a test section

Figure 2.1: Water tunnel used in current experiment.

with 2.5m of working length, and 45cm of width and depth.

2.2 Experimental apparatus

The present study focused on the hydrodynamics of an oscillating propulsor. A simplified geometry that involved a flat rectangular plate with blunt leading and trailing edges was considered. The plate was undergoing sinusoidal oscillatory motion with parameters that are specified in Table 2.1.

Three types of rectangular plate with a rigid upstream section and a flexible downstream section, as shown in Figures 2.2, with different ratios of rigid-to-flexible parts (1 : 0 - 100% rigid, 1 : 1 - 50%-rigid , 1 : 6 - 15%-rigid) were used to investigate the effect of chordwise flexibility on thrust coefficient C_t and efficiency η. All plate configurations had a span of 20cm, a chord length of 10cm, and a thickness of 1.6cm.

The plate was attached to the aluminium shaft, which in turn was connected to a 3-axial load cell. The 100% rigid plate and rigid parts for the plate with variable flexibility were produced by Prototype Equipment Design Inc, using acrylic. The flexible part was then produced in the lab by the molding process, using Polydimethylsiloxane (PDMS).

The rigid part of the plate was placed in front of the mold base, between the two side walls as shown in Figure 2.4. The mold end was then fixed to the end of two side walls to provide the casting volume with the rigid fin. An empty volume was

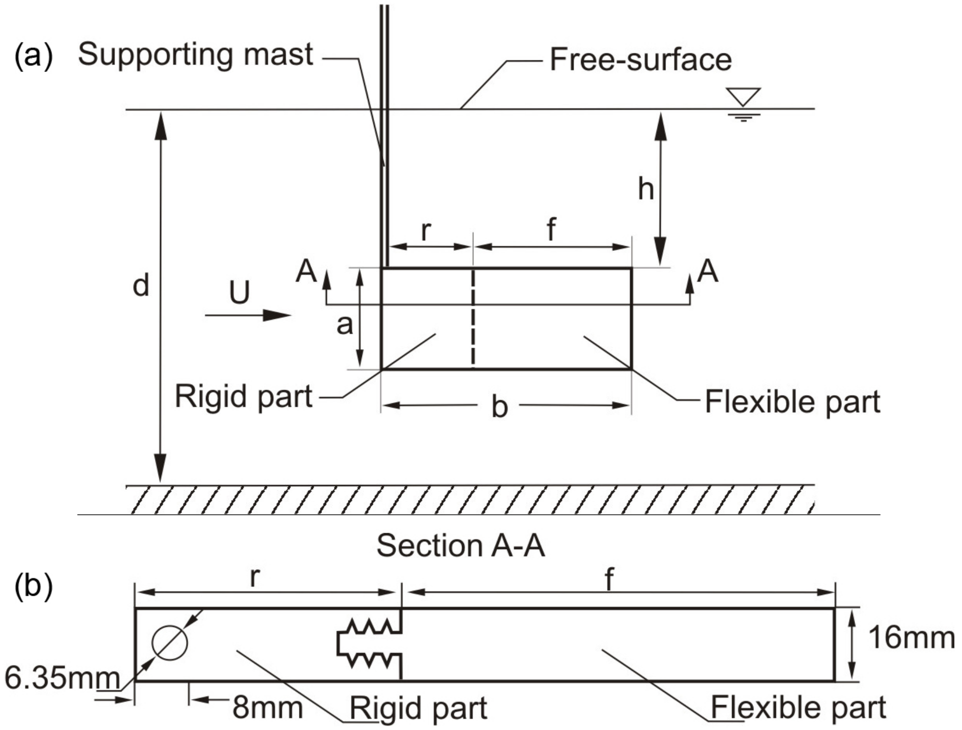

Figure 2.2: (a) Definition of principal dimensions for oscillating plate (b) Section A-A of the oscillating plate with chordwise flexibility

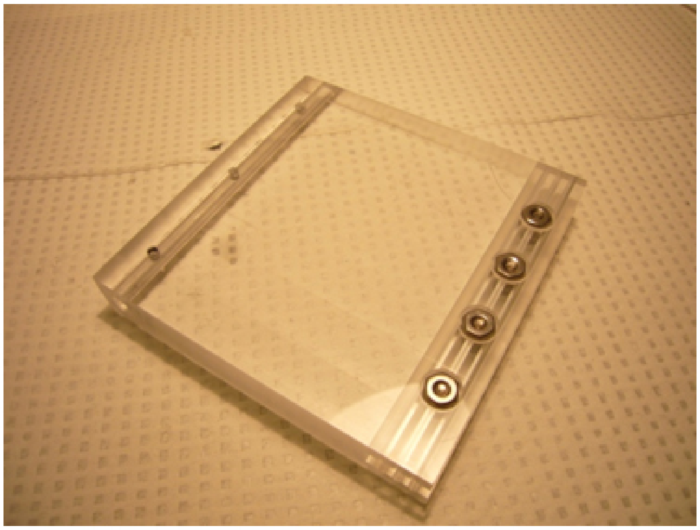

Figure 2.3: Example of a rigid part of the plate.

then formed for the PDMS to fill in. The liquid PDMS was gradually poured into the empty volume. When the whole volume was completely filled with PDMS, the mold base was precisely aligned, so that the top surface of the assembly was horizontal.

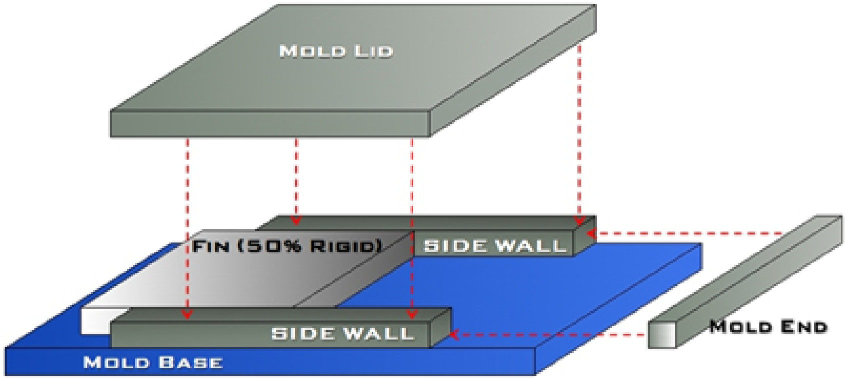

Figure 2.4: Schematics of the production process.

The mold filled with liquid PDMS was heated for approximately three hours at a temperature of 65°C. As the result of the molding process the flexible downstream part of the plate, made of the solidified PDMS, was permanently attached to the rigid upstream part.

2.3 Motion parameters and control

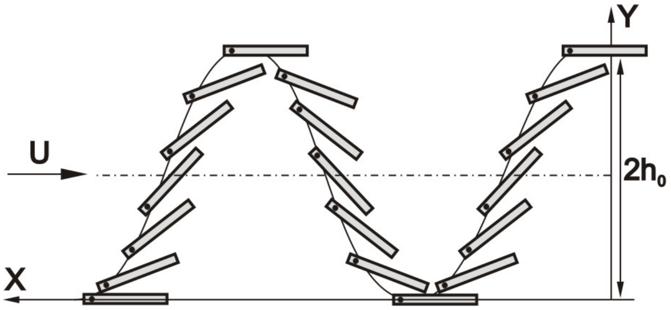

Figure 2.5: Trail of an oscillating plate showing amplitude $2h_0$.

In the present experiments, a rectangular plate with chord length c was undergoing a combination of heave and pitch motions ($h(t)$ and $\theta(t)$, respectively [35]), defined by equations (2.1) and (2.2).

$$h(t) = h_0 \sin(\omega t), \tag{2.1}$$

$$\theta(t) = \theta_0 \sin(\omega t + \psi), \tag{2.2}$$

Here ψ is the phase angle difference between pitch and heave motions, ω is the frequency of oscillation, h_0 is the amplitude of the heave motion, and θ_0 is the amplitude of pitch motion.

The choice of sinusoidal profile is based on analysis of underwater films of J. Cousteau, that were obtained in the natural habitat [5]. It was concluded that during uniform translatory motion, the trajectories of the stem and fin of a swimming dolphin are close to sine curve. It was also concluded by the authors that the pitch oscillations are lagging behind the heave oscillations by an angle close to $\psi = \pi/2$ which is referred as a phase angle.

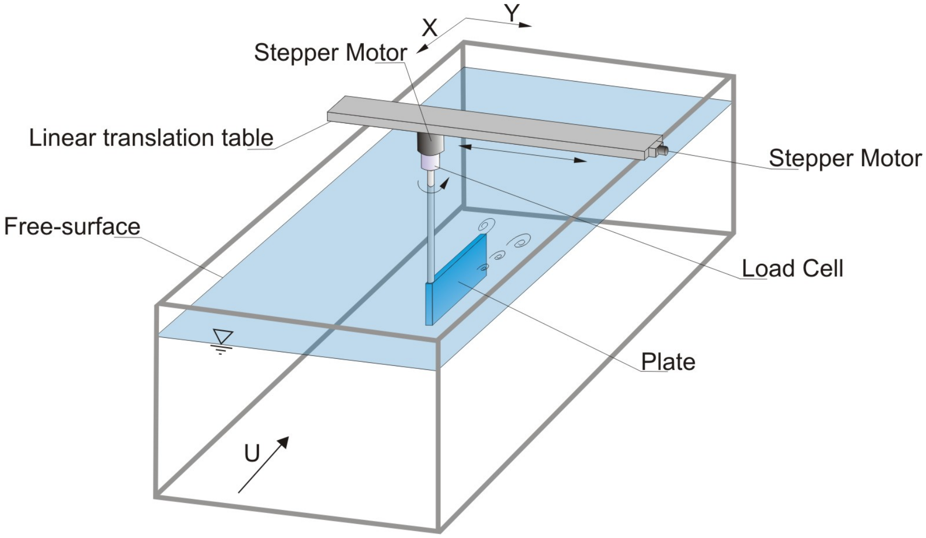

Figure 2.6: Schematics of the experimental setup.

The oscillating plate driving device, shown in Figure 2.6, was designed to be actuated linking heave direction motion with pitch direction motion by mounting the pitch direction driving device on the heave direction drive. A 2-axis motion control and positioning system is consisted of two *Parker HV23* stepper motors, and a linear table. Motors have a resolution of 25000 steps per revolution with an error 3 – 5% per step which is non cumulative from one step to another.

One stepper motor provided a heave motion through the Parker's HD series linear table with maximum travel distance of 1000mm and 60m/lb accuracy. Another motor connected to PEN-023-009-S7 Parker's Precision Gearhead with 9:1 gear ratio induced the pitch motion. Both motors were operated through 6K Series Controllers and motion profile was programmed using native 6K programming language.

Table 2.1 shows the values of the experimental parameters used in the present

Case	a (m)	b (m)	r (m)	f (m)	h (m)	d (m)	U (m/s)
A	0.1	0.2	0.2/0.1/0.03	0.0/0.1/0.17	0.00	0.45	0.22
B	0.1	0.2	0.2/0.1/0.03	0.0/0.1/0.17	0.08	0.45	0.22
C	0.1	0.2	0.2/0.1/0.03	0.0/0.1/0.17	0.17	0.45	0.22
D	0.1	0.2	0.2/0.1/0.03	0.0/0.1/0.17	0.25	0.45	0.22
E	0.1	0.2	0.2/0.1/0.03	0.0/0.1/0.17	0.33	0.45	0.22

Table 2.1: Parameters used for experiments on the effect free surface on propulsion characteristics of oscillating-foil system.

investigation, including the length of the rigid section of the plate r, the length of the flexible section f, the plate's width a, length b, the depth of the channel's test section d , the distance of the plate's top edge to free surface h, and the water tunnel velocity U.

2.4 Unsteady force measurements

To perform direct force measurements, a Novatech F233-Z3712 3-axial load cell was connected to the LabView through the 16-bit resolution Digital Acquisition system (DAQ). The acquisition frequency was set to 400Hz; this number was chosen based on expected operational frequencies of the system and in order to satisfy the sampling theorem [36]. Each experiment was recorded for 2 minutes, which yielded 48000 points. The duration of the experimental run made it possible to obtain from 20 to 72 full periods.

Force measurement accuracy tests were designed similarly to experimental runs. Test weights of $1N$, $4N$ and $8N$ were used as a control parameters for all three channels. In addition to that, an arm of $0.18m$ length was manufactured in order to test the torque channel M_z. For each weight the experiment was recorded for 2 minutes and then maximum and minimum values were evaluated. Due to low signal to noise ratio on F_x and F_y channels, which was the result from the combination of cabling, external voltage noise from stepper motors and power supply, and from the absence of amplifier near the output of the load cell, a rather high error of ±21% was documented. Meanwhile the torque channel M_z had an error of ±5% within the experimental range.

A LabView code, virtual instrument(vi), was developed to allow simultaneous recording of unsteady force signals from all three axes of the load cell as well as heave and pitch coordinates from the motion control and positioning system.

During experiments, various electronics interference was noticed. In order to minimize its influence on experimental result, it was decided to apply series of digital filters. High pass 3rd order filter with cut-off frequency of 0.2Hz and Chebyshev topology along with low-pass 10th order Butterworth filter with cut-off 10Hz were implemented in the Labview code and applied on the fly. In addition to that, a simple smoothing routine was written in Matlab and applied to the obtained data. Smoothing techniques are known to be efficient to reduce noise during data analysis in fields such as image processing, Doppler velocimetry, bridge monitoring or medical applications [37]. Eventually, the raw force data was postprocessed in Matlab by smoothing every 20 points in order to reduce the noise, the number 20 was chosen experimentally as an optimal one from the possible choice of 5-35 points average. The smoothing postprocessing however reduced effective acquisition frequency to 10Hz which still was sufficient enough to capture expected phenomenon.

2.5 Quantitative flow imaging

In order to investigate flow patterns around an oscillating flexible plate, particle image velocimetry (PIV) was used to measure two-dimensional velocity filed. Its schematics presented in Figures 2.7.

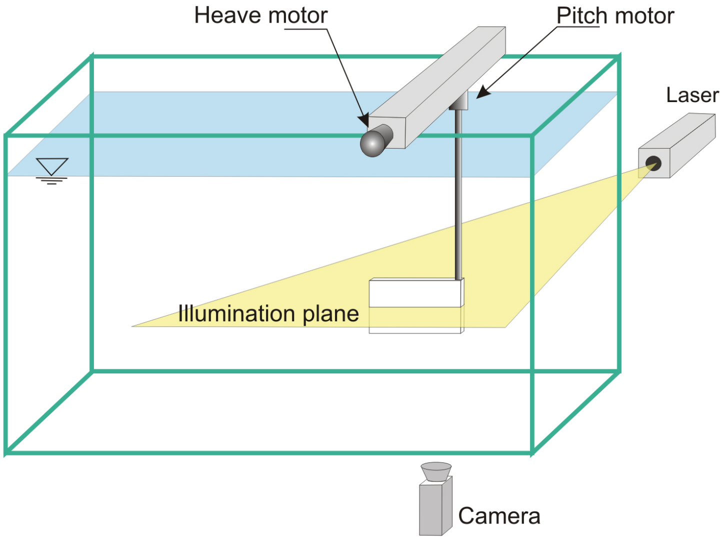

Figure 2.7: Schematics of PIV system.

Mearlin Supersparkle particles that contain the portions of Mica 12001-26-2 and

Titanium dioxide 1346-67-7, with mean diameter $5 - 7\mu m$, were used as a tracer particles. Even though the particles are not neutrally buoyant, their specific gravity is $2.9Kg/m^3$, the flow velocity in the water tunnel was high enough for them to stay in the flow.

The PIV system consisted of a 25 mJ Nd:YLF dual diode-pumped laser (Darvin-Duo series by Quatronix), that was used to produce a planar laser light sheet in order to illuminate the tracer particles, a 1024×1024 pixels CCD camera (HighSpeedStar HSS-5) and a PC equipped with hardware for PIV image acquisition. The light scattered by the tracers was captured by the digital camera in the vertical plane and sent to LaVision DaVis 7.2 software for data processing. The images were acquired with a rate of 300Hz, yielding 1000 frames; after that, the recorded sequence of images was evaluated using LaVision DaVis 7.2 software by cross-correlating pairs of frames, each containing single exposures of the group of tracers.

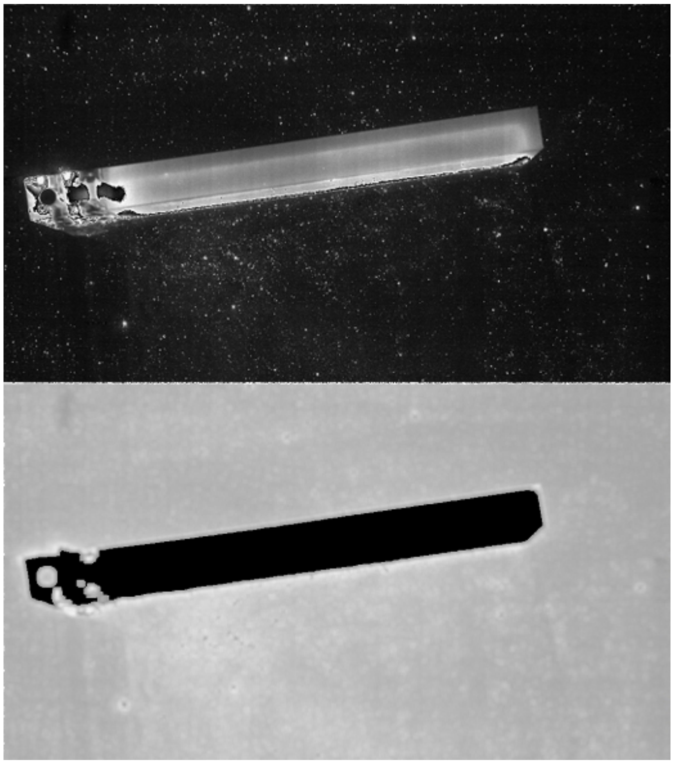

Figure 2.8: Plate before and after dynamic mask application.

In order to remove plate cross section from the field of view, an adaptive algorithmic mask was programmed in LaVision DaVis 7.2 software. The following steps were employed for plate's cross-section detection.

First, the suitable threshold was adopted in order to extract the plate from the background. In this step brightness and contrast were adjusted so that light distribution in the laser sheet, caused by the presence of water, was as much homogeneous as possible. In the next step the erosion operation was performed. It is known that erosion is a fundamental morphological operation that removes pixels from the boundaries of an object, hence reducing its size. In this step, the erosion operation was performed using 3×3 pixel square mask. During the next step the dilation operation, also a morphological operation that instead adds pixels to the object boundary, resulting in an increase of the object size was performed. The purpose of this operation here was to compensate for the area reduction of the objects due to the earlier erosion operation. Finally a 3 pixel smoothing was applied to level any irregularities that were left from the application of previous steps. All steps mentioned above were performed on every single frame, that complex operation resulted in masking out correctly the plate's cross section, which is shown as a black rectangle in Figure 2.8, from the field of tracer particles, shown as a light area in Figure 2.8.

After the plate's cross section had been removed, a multi-pass adaptive image interrogation algorithm was employed in order to improve the accuracy of the calculated velocity vectors by minimizing the loss of particle image pairs. The algorithm evaluated the particle images in several iterations. Initially, larger interrogation windows with the size of 128 pixels × 128 pixels were used to determine the local mean particle displacements. Subsequently, smaller interrogation windows were used to improve spatial resolution. The smallest interrogation window had the size of 12 pixels × 12 pixels.

By employing 50% overlap of the interrogation windows and a lens with a focal length of 40mm, the spatial resolution of the velocity vector field of 0.48 vectors/mm was obtained. Besides that, precision errors, which are associated with location of the particle displacement correlation peak, accounted for uncertainty of approximately 2.5%.

Chapter 3

Performance of the oscillating plate propulsor

3.1 Background

When a plate undergoes an oscillatory motion in the fluid according to the parameters specified in Section 2.3, it experiences the forces $F_x(t)$, $F_y(t)$ in the x- (forward) and y- (transverse, or lift) directions, respectively; and a torque $M_z(t)$. If T is the period of oscillation, the time-averaged value of $F_x(t)$, $\bar{F_x}$, and the average input power per cycle $\bar{P}$ are given by

$$\bar{F_x} = \frac{1}{nT}\int_0^{nT} F_x(t)dt, \tag{3.1}$$

$$\bar{P} = \frac{1}{nT}\left(\int_0^{nT} F_y(t)\frac{dh}{dt}(t)dt + \int_0^{nT} M_z(t)\frac{d\theta}{dt}(t)dt\right), \tag{3.2}$$

where n is a number of periods per run and it varies from 10 at $St = 0.10$ to 46 at $St = 0.46$. The force data were reduced to thrust and power coefficient respectively using the following equations [35]:

$$C_T = \frac{\bar{F_x}}{\frac{1}{2}\rho c s U^2} \tag{3.3}$$

$$C_P = \frac{\bar{P}}{\frac{1}{2}\rho c s U^3}, \tag{3.4}$$

where c and s are the chord and the span of the plate, respectively, and ρ is the density of the fluid.

The propulsive efficiency is defined as a ratio of useful power over input power, and is given by

$$\eta_P = \frac{\bar{F}_x U}{\bar{P}}, \tag{3.5}$$

hence $\eta_P = C_T/C_P$.

One of the most important parameters related to the oscillatory plate motion is the Strouhal number based on the heave amplitude. The Strouhal number is defined as follows

$$St = \frac{fA}{U}, \tag{3.6}$$

where f denotes the frequency of foil oscillation in Hz(tailbeat frequency of the fish), that is $f = \omega/(2\pi)$, and A is a characteristic width of the created jet flow, which will be discussed later in this section. The last parameter was not known in advance and, following [38], was taken to be equal to the double of the heave amplitude, i.e. $A = 2h_0$.

Throughout the all experiments, the incoming velocity U was set to 0.22 m/s, resulting in a Reynolds number $Re = Uc/\nu$ of 44000, which is close the Reynolds number $Re = 45000$ estimated for a striped mullet [38]. The amplitude of the heave motion h_0 was set to $0.08m$ and the amplitude of the pitch motion θ_0 was set to $8°$. Moreover, this investigation was limited to a phase difference ψ between the heaving and pitching motions equal to $90°$, which corresponds to the optimum propulsion as reported in previous experimental studies [35], [12], [39]. Therefore, the parametric study involved variation of the oscillating frequency f in order to obtain the necessary range of Strouhal number St, which varied in our case between 0.10 and 0.46 with an increment of $\Delta St = 0.02$.

Figure 3.1 illustrates an example of the simultaneous time recordings of the $F_x(t)$ and $F_y(t)$ force components, along with heave position $h(t)$ and pitch angle $\theta(t)$. It can be seen from these graphs that, while the vertical force F_y exerted on the plate is alternatively positive and negative, the horizontal force component F_x is generally positive during the upward and the downward heave motion. As the result, the frequency of $F_x(t)$ is twice the value of the frequency of the plate oscillation. In the present case, the force F_x does become negative for brief periods of time in each cycle, which means that during that period of time oscillating plated produced drag.

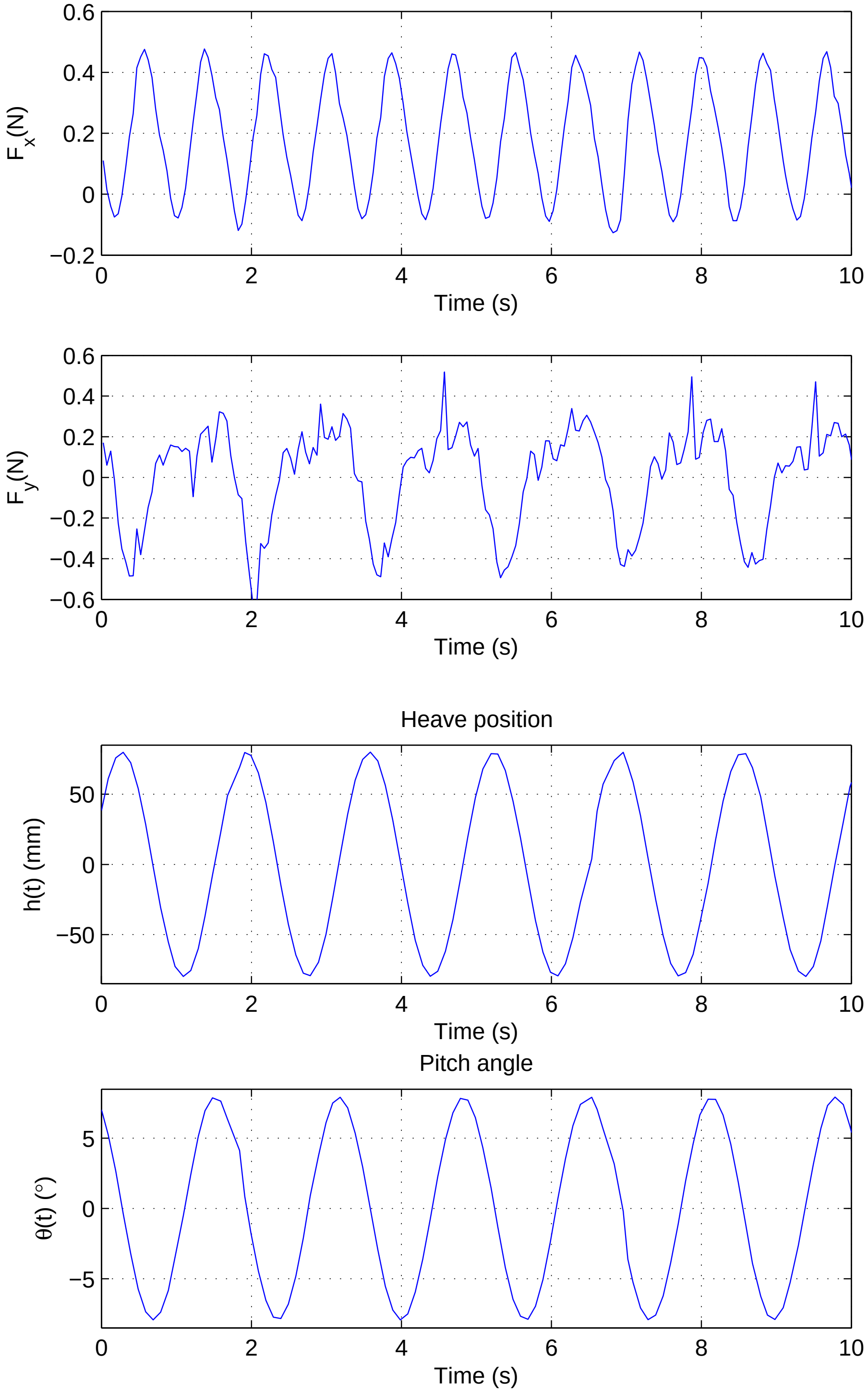

Heave position

Pitch angle

Figure 3.1: Time recording of the instantaneous forward F_x and transverse F_y force components, heave and pitch position for $St = 0.44$ and $\theta_0 = 8°$.

The maximum values of F_x and the extrema of F_y were observed when the heave velocity $\dot{h}$ and the pitch angle θ were at their maximum, that is $h = 0$ and $\theta = \theta_0$. Both force components reached zero values when the heave velocity vanished: $h = \pm h_0$ and $\theta = 0°$.

3.2 Effect of chordwise flexibility of the oscillating plate

3.2.1 Thrust coefficient

In Figure 3.2, one can see the overall result of experimentally obtained values of thrust coefficient C_t, which is defined in equation (3.3), as a function of the Strouhal number, $St = fA/U$, defined according to equation (3.6). The data corresponds to the depth of submergence $h_0 = 0.8cm$ (defined in Figure 2.2) and 90° phase angle between the heave and the pitch motions. The heave and the pitch motions of the plate were varied sinusoidally with a frequency of oscillations ranging between $0.17Hz$ to $0.63Hz$, corresponding to the range of Strouhal number St $[0.10 - 0.44]$ with $\Delta St = 0.02$.

It can be seen on the graph of the thrust coefficient C_t, that its value increases uniformly with Strouhal number St. This observation coincides with the results obtained in the similar experiments by [40], [38] and [6]. As the frequency of oscillation increases, the system reaches a critical point where the oscillating plate begins to generate thrust, which corresponds to the value of Strouhal number $St \approx 0.25$. This phenomenon corresponds to the following structure of the wake generated by the plate. At the critical value of the Strouhal number, an alternating vortex pattern is formed such that the vortex with a positive (counter-clockwise) circulation is shed at the top position and the vortex with the negative (clockwise) circulation is shed at the bottom position in terms of the heave trajectory.

This structure is an inverse of the well known von Kármán vortex street, that can be observed in wakes, and corresponds to the formation of an average velocity profile in the form of a jet. Hence the critical value of Strouhal number St correspond to the transformation of the wake of the oscillating propulsor from a regime corresponding to a net momentum deficit to the regime corresponding to a net momentum excess, thus producing thrust.

It can be noted that the critical value of the thrust coefficient was not the same

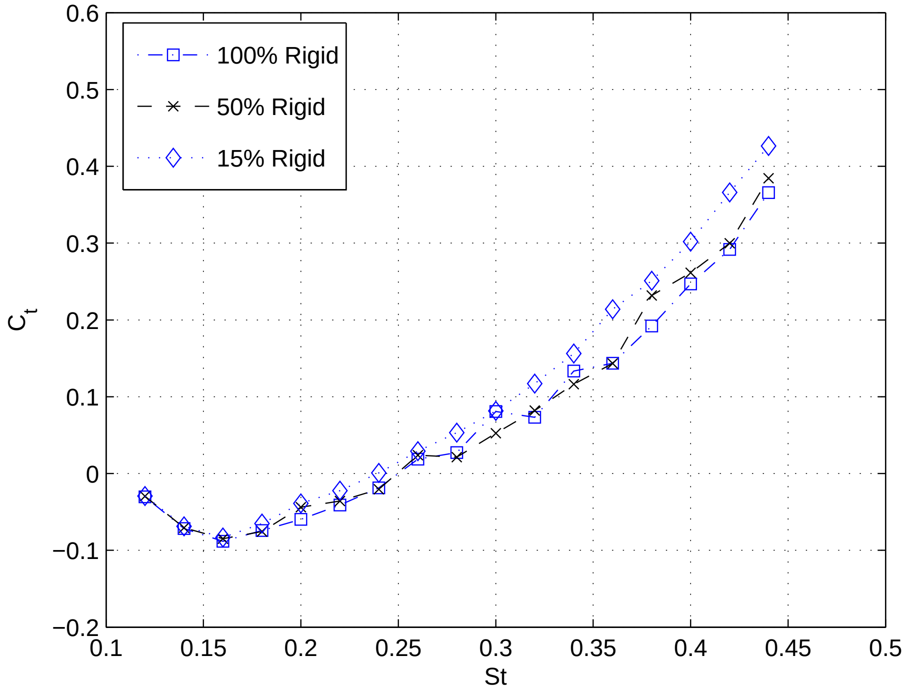

Figure 3.2: Experimentally measured thrust coefficient C_t as a functions of Strouhal number St for three types of flexible plates, $1 : 0$ ratio: $h = 17cm$, $r = 20cm$, $f = 10cm$, $\alpha_{\max} = 8°$, $h_0 = 8cm$, $\varphi = 90°$; $1 : 1$ ratio: $h = 17cm$, $r = 10cm$, $f = 0cm$, $\alpha_{\max} = 8°$, $h_0 = 8cm$, $\varphi = 90°$; $1 : 6$ ratio: $h = 17cm$, $r = 3cm$, $f = 17cm$, $\alpha_{\max} = 8°$, $h_0 = 8cm$, $\varphi = 90°$.

for all three plates. The most flexible plate with $1 : 6$ rigid-to-flexible ratio started to produce thrust at slightly lower value of the Strouhal number $St \approx 0.24$ than the other two plates. This critical value not only depends on the chordwise flexibility of the plate, but also on the ratio of heave amplitude h_0 to chord length c, and on the value of maximum angle of attack α_{max} as was shown in [12]. According to [12], zero crossing can vary from a very low Strouhal number $St = 0.10$ for $h_0/c = 1.0$ and $\alpha_{max} = 10 - 15°$ to a rather moderate value of Strouhal number $St = 0.32$ for $h_0/c = 0.75$ and $\alpha_{max} = 50°$. From Figure 3.2 it is clear that the most flexible plate with $1 : 6$ rigid-to-flexible ratio provided more thrust than the the plates with $1 : 1$ and $1 : 0$ rigid-to-flexible ratios respectively in propulsion regime, which corresponds to the range of Strouhal number St $[0.24 - 0.44]$. This range is in the good agreement with the range of $[0.25 - 0.4]$ reported by [38].

Starting at a zero crossing on the thrust coefficient curves, average percentage increase of thrust coefficient C_t for the plate with $1 : 1$ rigid-to-flexible ratio compared to the plate with 1 : 0 rigid-to-flexible ratio was equal to 13% and for the plate with 1 : 6 rigid-to-flexible ratio compared to the plate with 1 : 0 rigid-to-flexible ratio it was equal to 27%. During the trust-generating regime, the value of thrust coefficient C_t increased with the increase of the Strouhal number and agreed with results reported by [23] and [41]. It can be concluded that, when properly selected, the chordwise flexibility can lead to an increase in thrust coefficient.

3.2.2 Efficiency

In Figure 3.3, plots of efficiency as a function of time, obtained for the same range of the motion parameters as the ones for the thrust coefficient C_t, are presented. The maximum values for the efficiency for all three cases are 48%, 34% and 27% for the plates with 1 : 6, 1 : 1 and 1 : 0 rigid-to-flexible ratios respectively. Those peaks occur in the range of the Strouhal number St $[0.25 - 0.35]$, confirming that the maximum efficiency is achieved in the range suggested by [38].

Each curve in Figure 3.3 corresponds to the efficiency evolution for one of possible three choices of plate with 1 : 6, 1 : 1 and 1 : 0 rigid-to-flexible ratios. As with the thrust coefficient C_t, the efficiency of 1 : 6 rigid-to-flexible ratio plate is higher than that of the other two plates. This can be explained if one considers the change of the plate's curvature along its path, as was proposed in [18]. It can be seen that with the increase of the curvature of the plate, caused by forced heave and pitch motions, instantaneous lift decreases, however the orientation of the resulting lift is nearer the direction of advance, which in turn suggests higher efficiency.

However, the high efficiency peaks that were obtained, correspond to relatively low value of thrust coefficient C_t, (less then 0.1) for all three cases and hence have limited relevance for propulsion applications. Similar results were reported by [12], where maximum efficiency of 75% was found. However, this value was achieved at the value of the Strouhal number for which the thrust coefficient was equal to 0.16. In the range of St corresponding to the high C_t, the efficiency of the oscillating propulsor was found to be approximately 55% [12].

The difference between the results reported in [12] and those of the present investigation is most importantly due to the geometry of the plate. Sharp corners at the leading edge of the plate produce flow separation, which in turns results in strong reduction of the suction force component leading to the rapid decrease in efficiency. The importance of avoiding such scenario, when flapping foil propulsion is greatly influenced by leading edge flow separation, was first pointed out in [13]. Intensive numerical study of the effects of dynamic stall on propulsive efficiency in [42] converged to the same conclusion. The authors reported a rapid decrease in efficiency when the leading edge flow separation was observed. However leading edge flow separation does not always cause a rapid drop in the efficiency. Anderson in [35] showed experimentally that under the right parameter values there is a constructive interaction of the leading and trailing edge vortices, which in turn improves the propulsive performance.

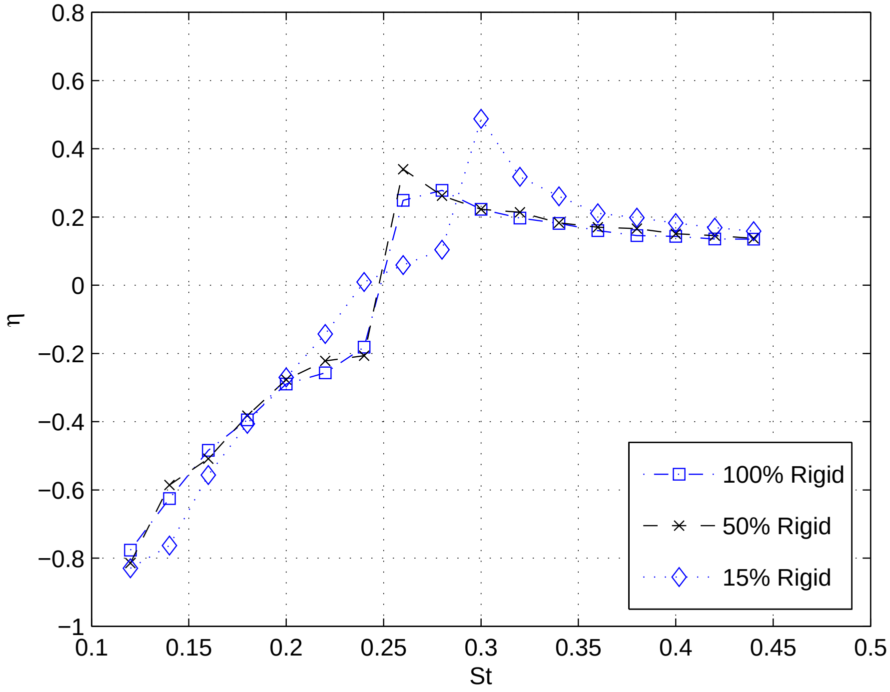

Figure 3.3: Experimentally measured efficiency η as a functions of Strouhal number St for three types of flexible plates, $1:0$ ratio: $h = 17cm$, $r = 20cm$, $f = 10cm$, $\alpha_{\max} = 8°$, $h_0 = 8cm$, $\varphi = 90°$; $1:1$ ratio: $h = 17cm$, $r = 10cm$, $f = 0cm$, $\alpha_{\max} = 8°$, $h_0 = 8cm$, $\varphi = 90°$; $1:6$ ratio: $h = 17cm$, $r = 3cm$, $f = 17cm$, $\alpha_{\max} = 8°$, $h_0 = 8cm$, $\varphi = 90°$.

Other differences between the current results and those reported in [12] are mainly due to the type of propulsor used and different amplitude to chord ratios. The latter parameter in particular, as indicated by [18] and experimentally verified by [12] and [39] has significant impact on thrust coefficient C_t and efficiency η. Ideally, for a propulsion system one requires high efficiency in conjunction with high thrust, and in Figure 3.3 one can see that efficiency tangentially approaches a value of $\approx 18\%$ in the range of Strouhal number St $[0.35 - 0.40]$. This interval corresponds to higher values of thrust coefficient C_t and hence is more applicable.

Yamamoto et al. in [41] performed similar experiments on a ship model equipped with harmonically oscillating propulsion mechanism. The authors tested fins of different chordwise flexibility and showed that the fin with 1 : 6 rigid-to-flexible ratio, achieved the better overall efficiency of 31% then the other 6 prototypes reported in the article. Comparing the results obtained in [41] with those reported here, it can be seen that the most flexible plate with 1 : 6 rigid-to-flexible ratio also performed better then the other two. It was possible to achieve as much as 48% efficiency for the plate with 1 : 6 rigid-to-flexible ratio. Hence it can be concluded that increase in chordwise flexibility leads to the increase in propulsive efficiency.

3.3 Variation of heave amplitude and its influence on thrust and efficiency

The next step was to consider fixed values of the forcing frequency corresponding to the peak values of Strouhal number on the efficiency curves for each of the plates and vary the heave amplitude in such a way that the Strouhal varies in the range of $St \in [0.10,\ 0.44]$. This approach, combined with the experiments that involved variation of the oscillation frequency at a fixed value of heave amplitude, provides additional insight into performance of an oscillating plate as a propulsor. From Figure 3.3, the maximum values of the efficiency for all three cases are 48%(at St = 0.3), 34%(at St = 0.26) and 27%(at St = 0.28) for 1 : 6, 1 : 1 and 1 : 0 rigid-to-flexible ratio. For these values of Strouhal number, the corresponding values of heave oscillating frequencies are 0.41Hz, 0.36Hz and 0.29Hz for 1 : 6, 1 : 1 and 1 : 0 rigid-to-flexible ratio plates.

The peak-to-peak amplitude of plate oscillation was varying in the range of $h_0 =$ [64mm –236mm] for 1 : 6 rigid-to-flexible ratio plate, [73mm – 269mm] for 1 : 1 rigid-to-flexible ratio plate and [68mm – 248mm] for 1 : 0 rigid-to-flexible ratio plate. The plots of thrust coefficient and efficiency are presented in Figure 3.4 and Figure 3.5, respectively.

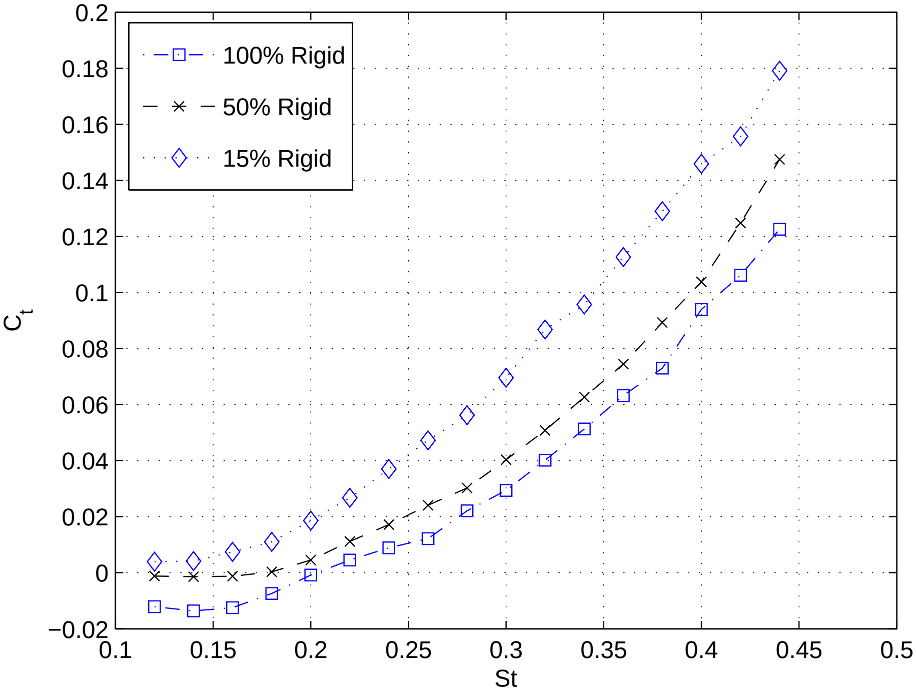

Figure 3.4: Experimentally measured thrust coefficient C_t as a functions of Strouhal number St for three types of flexible plates, $1:0$ ratio: $h = 17cm$, $r = 20cm$, $f = 10cm$, $\alpha_{\max} = 8°$, $h_0 \in [6.4cm, 23.6cm]$, $\varphi = 90°$; $1:1$ ratio: $h = 17cm$, $r = 10cm$, $f = 0cm$, $\alpha_{\max} = 8°$, $h_0 \in [7.3cm, 26.9cm]$, $\varphi = 90°$; $1:6$ ratio: $h = 17cm$, $r = 3cm$, $f = 17cm$, $\alpha_{\max} = 8°$, $h_0 \in [6.8cm, 24.8cm]$, $\varphi = 90°$.

3.3.1 Thrust coefficient

From the graph of the thrust coefficient C_t, one can see that the general dynamics in the behavior is similar to the results presented in Figure 3.2, thrust increases almost linearly starting from $St = 0.17$. However, on this graph it was possible to capture more details on differences between the performances of the three plates. It can be seen that for the lowest value of the Strouhal number the most flexible plate, with $1:6$ rigid-to-flexible ratio, starts producing positive thrust from the very beginning.

The next plate under consideration is the one with $1:1$ rigid-to-flexible ratio. It can be observed that for the smallest value of the amplitude it does not produce any thrust and rather sits at zero. However, with the increase of oscillating amplitude on the heave axis one can see that plate starts to produce positive thrust at $St = 0.18$ and continues to do that through all of the data set. The plate with $1:0$ rigid-to-flexible ratio does tend to produce negative thrust up to the value of the Strouhal number of $St = 0.2$, after that with almost the same slope as in the previous two cases, it produces positive thrust. Comparing these plots, with those presented in Figure 3.2, it can be concluded that spanwise flexibility does affect the thrust production in a positive way. The most flexible plate that was used in this sets of experiments produced higher thrust. Besides that, with fixed optimal frequency of oscillation, the most flexible plate started to produce thrust faster then the other two plates, and at the lowest values of oscillating amplitude.

3.3.2 Efficiency

Using the same range of parameters, the efficiency curves plotted from experimental data are presented in Figure 3.5. One can see that the shape of the graphs is topologically similar to the ones presented in Figure 3.3. Three distinct regimes can be observed. The regime of gradual increase of efficiency for each of the plates lasts until efficiency reaches its maximum value. The regime of maximum efficiency, the value of Strouhal number at which the efficiency is maximum, and the regime of gradual decrease where the efficiency decreases with the increase of Strouhal number and eventually asymptotically reaches the limiting value.

It can be seen that the data obtained from the change of heave amplitude, adjusted so that the range of Strouhal number is the same as in the case when the amplitude was fixed, gives good understanding on propulsive differences between the three plate designs. By combining graphs from experiment 1, where the oscillating frequency was varying, along with experiment 2, where the amplitude of oscillation was varying, the observation similar to one from the analysis of thrust curves can be presented. Clearly, all three plates have a very different impact on efficiency performance of the propulsion system. As in the case with thrust coefficient, the most rigid plate started to operate in the negative regime. As the chordwise flexibility increased, by changing the type of the plate to the one with 1 : 1 rigid-to-flexible ratio, it can be seen that second plate produced zero efficiency for two values of oscillating amplitude and then makes efficiency grow as the value of Strouhal number increases. However, the most flexible plate already starts at 15% efficiency value for the smallest value of heave amplitude, and continues to produce positive efficiency with the increase of the Strouhal number. It can be concluded from the graphs presented in Figures 3.2 − 3.5 that the Strouhal number, oscillating frequency and heave amplitude triplets such as $\{St = 0.3, f = 0.41Hz, h_0 = 16.1cm\}$,$\{St = 0.26, f = 0.36Hz, h_0 = 15.9cm\}$ and

$\{St = 0.28, f = 0.29Hz, h_0 = 15.8cm\}$for 1 : 6, 1 : 1 and 1 : 0 rigid-to-flexible ratio plates respectively, are the optimal parameter combinations that allow oscillating plate propulsion system to operate in thrust-producing regime with highest efficiency.

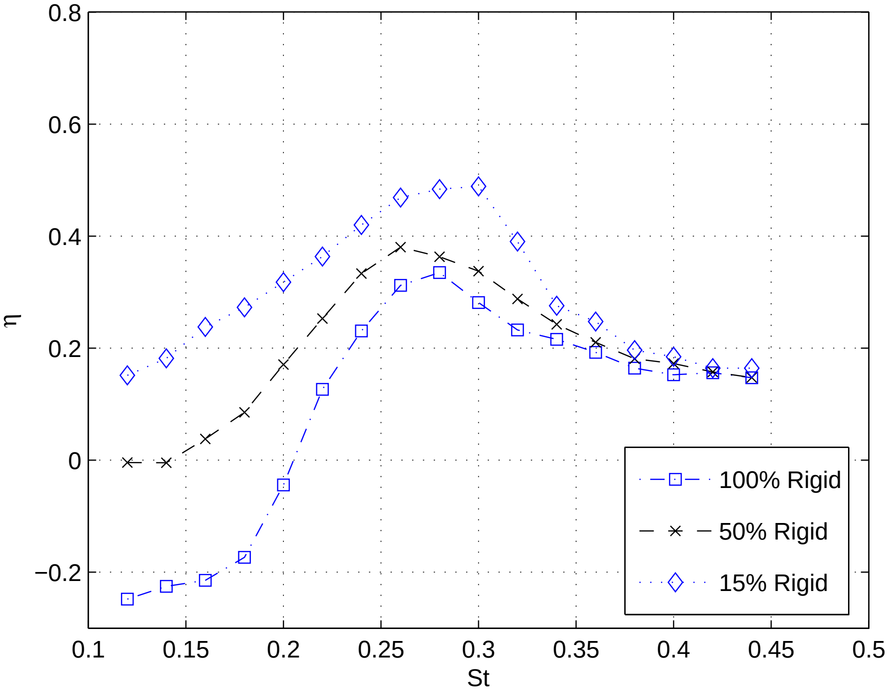

Figure 3.5: Experimentally measured efficiency η as a functions of Strouhal number St for three types of flexible plates, 1 : 0 ratio: $h = 17cm$, $r = 20cm$, $f = 10cm$, $\alpha_{\max} = 8°$, $h_0 \in [6.4cm, 23.6cm]$, $\varphi = 90°$;1 : 1 ratio: $h = 17cm$, $r = 10cm$, $f = 0cm$, $\alpha_{\max} = 8°$, $h_0 \in [7.3cm, 26.9cm]$, $\varphi = 90°$; 1 : 6 ratio: $h = 17cm$, $r = 3cm$, $f = 17cm$, $\alpha_{\max} = 8°$, $h_0 \in [6.8cm, 24.8cm]$, $\varphi = 90°$.

3.4 Depth of submergence and its influence

When the plate is oscillating in an unbounded fluid the horizontal thrust is equals to the mean momentum transport in the vortex wake which is formed behind the plate. From this it follows that the wasted energy is mainly due to the wake. When a free surface is present, the problem becomes much more complicated, especially because the waves always give rise to a considerable amount of wasted energy. The plate in close proximity to a free surface will generate surface waves that may transport large amount of momentum downstream. Depending on the properties of generated waves, this momentum transport might be either positive or negative. This in turns will lead to an increase or decrease in thrust and efficiency.

In order to investigate the effect free surface on propulsion characteristics of oscillating-foil system the test section of the water tunnel was divided into five experimental depths, as shown in Table 1.

3.4.1 Thrust coefficient

In Figures 3.6 – 3.8 detailed experimental investigation of the propulsive characteristics of an oscillating plate for different experimental depths is presented. Range of parameters used in experiments is presented in Table 2.1. Comparison of the measured thrust coefficient C_t near bottom of the channel (Case E) in middepth (Case C) and near free surface (Case A) and in intermediate cases showed that the plate oscillating near channel floor has a larger thrust over almost the whole range of Strouhal number which was used. Remarkably, it was found that operating the plate near water surface (Case B) changes the thrust only slightly from the value produced at middepth (Case C).

Due to the position of the plate, i.e. in a vertical plane, the dependance of the thrust coefficient on the depth of submergence is limited, because only the upper part of the plate interacts with free surface while most of the plate stayed submerged. However, since the span length in our case is not very large as well, surface patterns still affect propulsive characteristics of the plate, even though not as strongly as for the horizontally submerged plate.

This results confirm theoretical study done by Grue et al. in [22]. The authors found that the energy waste due to generated surface waves is a dominant part of the waste and increasing of submergence depths leads to the increase in thrust. Similar observations were reported in [23]. The authors noticed that influence of the foil generated free surface waves is different for the foils of different aspect ratios. The foil with small aspect ratio generates larger free surface effects than those created by a foil with larger aspect ratio. Thus, the reduction of thrust and efficiency due to induced drag is more pronounced for the foil with small aspect ratio.

When the plate was positioned tangent to the free surface, the variation in the thrust coefficient C_t was different from that for all cases considered earlier. One can see that starting at $St \approx 0.30$ for plates of all types of chordwise flexibility, there is a steep rise in thrust coefficient, whilst the efficiency asymptotically approaches its limit.

It is possible to highlight two physical mechanisms behind this phenomenon. When the plate undergoes periodic oscillations, part of the waves generated propagates in the same direction as the plate's translation, these will induce drag on the plate. However, there will be waves that propagate in the opposite direction, and those ones will generate thrust. Hence, the magnitude of those propagating waves will affect the overall thrust. Another possibility lies in the interaction between free surface waves and vorticity wake. It is possible that for the range of the Strouhal number, $St = [0.30-0.45]$, the energy of the bow wave, created by the leading edge of the plate, is absorbed by the trailing edge in the process of wake generation which will lead to increase in thrust. In order to provide the correct answer regarding the mechanism of this phenomenon, further investigations are required.

3.4.2 Efficiency

Plots of the efficiency for various chordwise flexibilities are shown in Figures 3.6 – 3.8. Similarly to the results for the thrust coefficient C_t, the overall improvement of the efficiency η with the increase of submergence depth was observed.

Comparing plots for the plates with $1:0$ and $1:1$ rigid-to-flexible ratio respectively, it can be seen that cases A, B and C on the range of the Strouhal number $St = [0.10 - 0.22]$ where both thrust and efficiency are negative, which means that plate produces drag, and $St = [0.30 - 0.45]$ is the range that corresponds to the highest thrust, mostly coincide with each other. Case C for the plate with $1:6$ rigid-to-flexible ratio behaved differently and showed substantial increase in efficiency. This phenomenon can be credited to the improvement of lift direction, caused by the curvature of the large area of the plate, as was proposed in [18]. According to the authors of [18], it leads to the efficiency increase.

Zhu in [23] noticed that the influence of foil generated free surface waves is different for foils of different aspect ratios. In small aspect ratio, when $s/c = 1$ the reduction of thrust and efficiency due to induced drag also comes along with much larger free surface effects, than those created by a foil with aspect ratio $s/c = 5$. Zhu reported that for large aspect ratio foil the maximum changes caused by free surface in thrust and efficiency are 3% and 11% respectively. While the effect of free surface on a small aspect ratio foil leads to reduction of 8% and 40% on thrust and efficiency. The plate presented in current experiments has a small aspect ratio $s/c = 0.5$, and from the Figures 3.6 – 3.8 a reduction of more than 44% for thrust coefficient and 66% for efficiency can be observed. It follows that small aspect ratio foils are more sensitive to the free surface effects.

Another interesting result can be seen on the efficiency plots for all types of plate. It is the highest value of efficiency near the bottom of the water channel (Case D) and (Case E). This can be contributed to the so called ground effects, similar to those experienced by high-speed ground vehicles, birds and bottom-dwelling fishes. It can be concluded that ground effect in our case leads to an increase in propulsive efficiency. Similar conclusion was reached by [43] in his theoretical investigation of ground effect on propulsion of birds and fishes.

Comparing the plots for the propulsive characteristics for the plates of variable flexibility, presented in Figures 3.6 − 3.8, it can be seen that the elastic plate with 1 : 6 rigid-to-flexible ratio can produce 7% more thrust compared to the plate with 1 : 0 rigid-to-flexible ratio, for identical geometric and kinematic parameters. This confirms conclusions of the previous section, that thrust coefficient increases with the increase of chordwise flexibility of the plate.

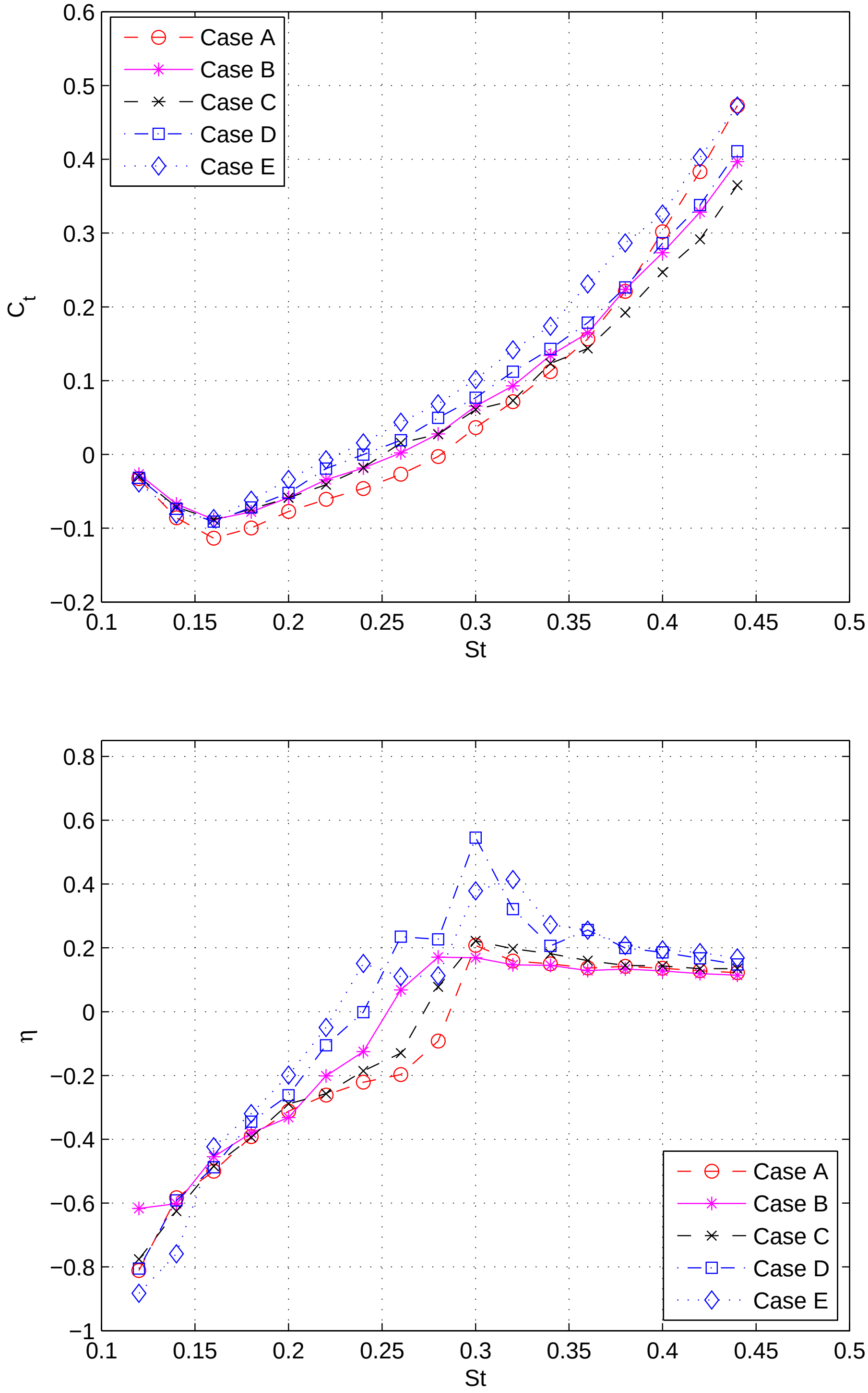

Figure 3.6: Experimentally measured thrust coefficient and efficiency as a function of Strouhal number St for $1:0$-ratio plate. Case A: $h = 0cm$, $r = 20cm$, $f = 0cm$, $\alpha_{\max} = 8°$, $h_0 = 8cm$, $\varphi = 90°$; case B: $h = 8cm$, $r = 20cm$, $f = 0cm$, $\alpha_{\max} = 8°$, $h_0 = 8cm$, $\varphi = 90°$; case C: $h = 17cm$, $r = 20cm$, $f = 0cm$, $\alpha_{\max} = 8°$, $h_0 = 8cm$, $\varphi = 90°$; case D: $h = 25cm$, $r = 20cm$, $f = 0cm$, $\alpha_{\max} = 8°$, $h_0 = 8cm$, $\varphi = 90°$; case E: $h = 33cm$, $r = 20cm$, $f = 0cm$, $\alpha_{\max} = 8°$, $h_0 = 8cm$, $\varphi = 90°$.

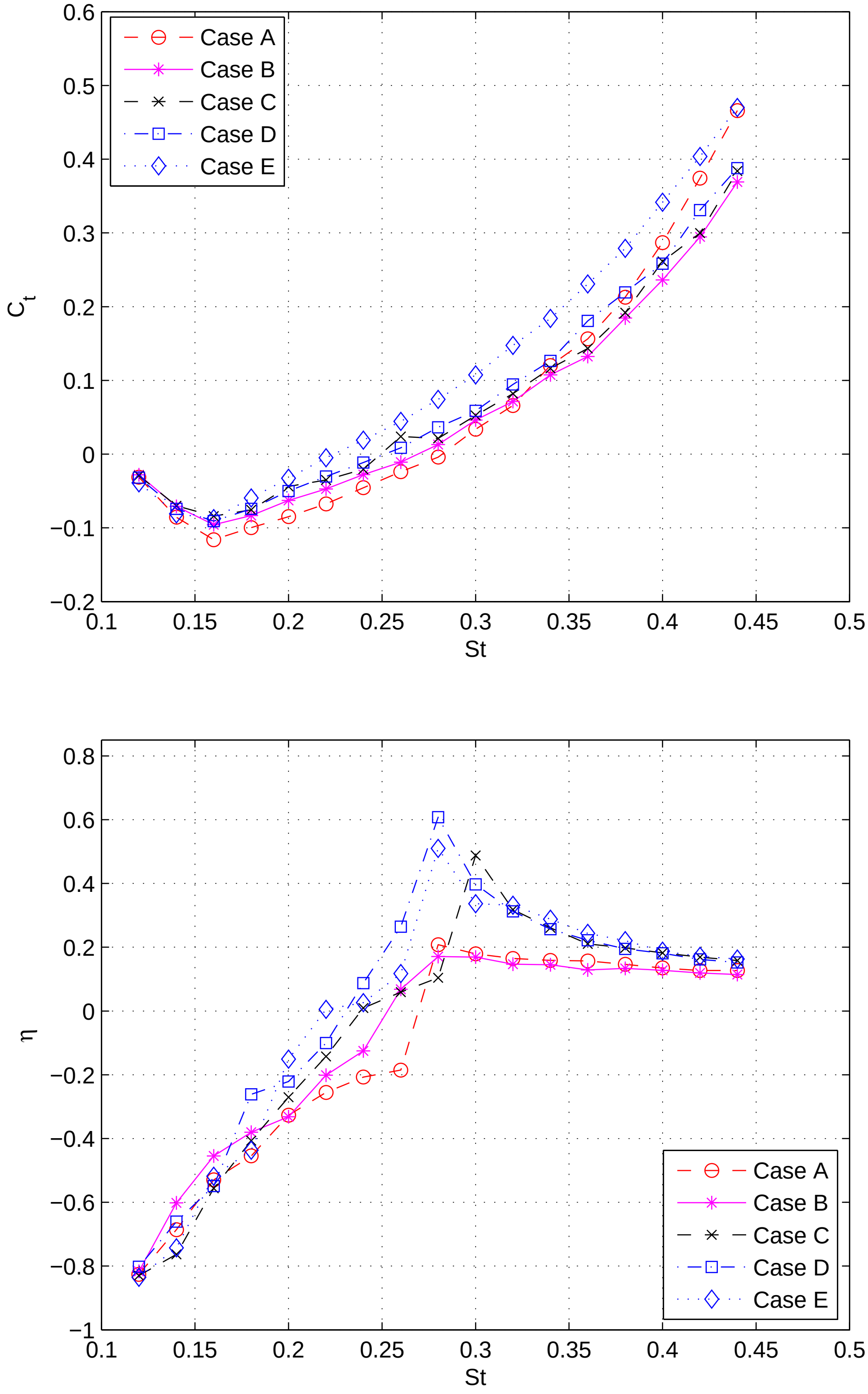

Figure 3.7: Experimentally measured thrust coefficient and efficiency as a function of Strouhal number St for 1 : 1-ratio plate. Case A: $h = 0cm$, $r = 10cm$, $f = 10cm$, $\alpha_{\max} = 8°$, $h_0 = 8cm$, $\varphi = 90°$; case B: $h = 8cm$, $r = 10cm$, $f = 10cm$, $\alpha_{\max} = 8°$, $h_0 = 8cm$, $\varphi = 90°$; case C: $h = 17cm$, $r = 10cm$, $f = 10cm$, $\alpha_{\max} = 8°$, $h_0 = 8cm$, $\varphi = 90°$; case D: $h = 25cm$, $r = 10cm$, $f = 10cm$, $\alpha_{\max} = 8°$, $h_0 = 8cm$, $\varphi = 90°$; case E: $h = 33cm$, $r = 10cm$, $f = 10cm$, $\alpha_{\max} = 8°$, $h_0 = 8cm$, $\varphi = 90°$.

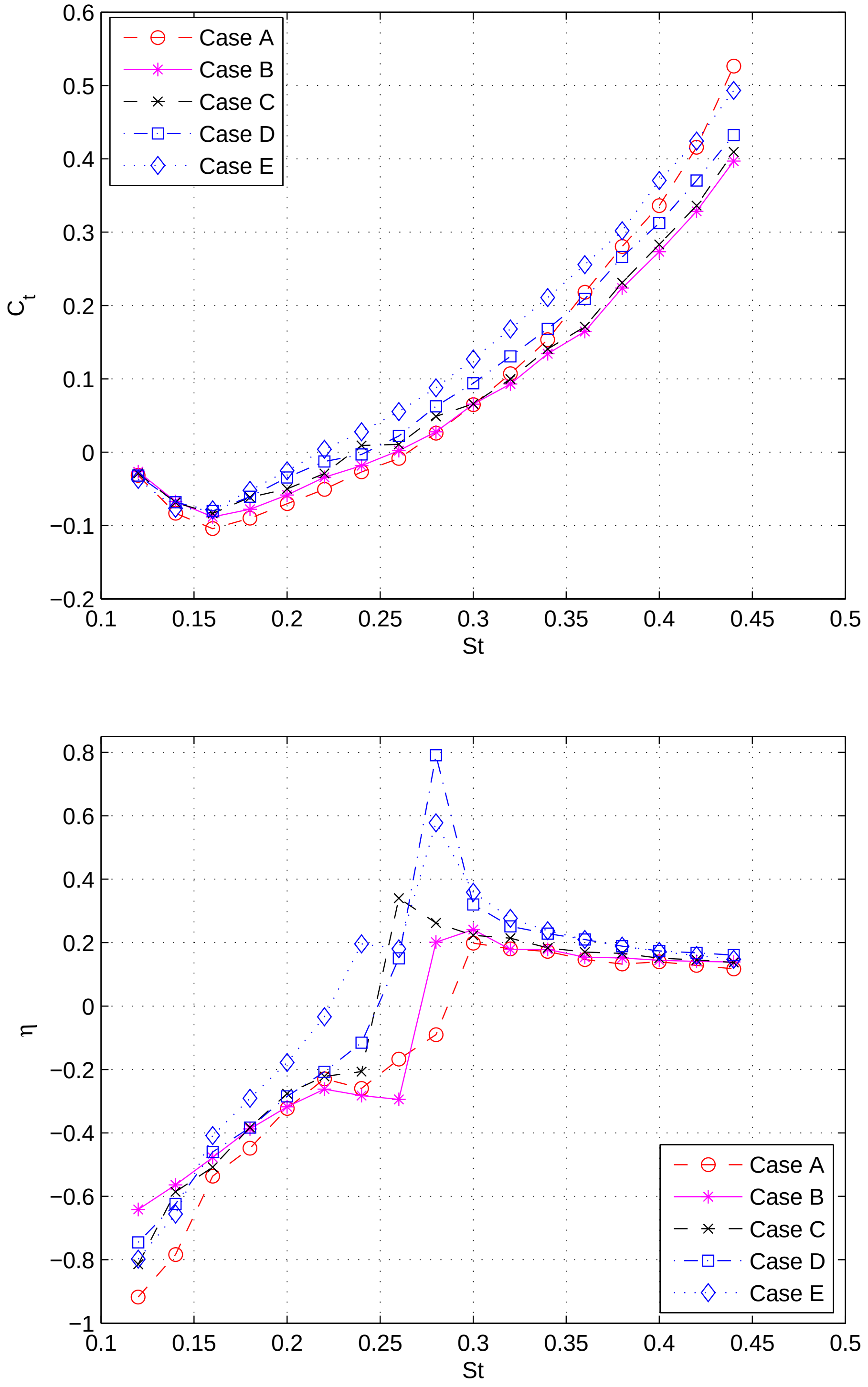

Figure 3.8: Experimentally measured thrust coefficient and efficiency as a function of Strouhal number St for 1 : 6-ratio plate. Case A: $h = 0cm$, $r = 3cm$, $f = 17cm$, $\alpha_{\max} = 8^\circ$, $h_0 = 8cm$, $\varphi = 90^\circ$; case B: $h = 8cm$, $r = 3cm$, $f = 17cm$, $\alpha_{\max} = 8^\circ$, $h_0 = 8cm$, $\varphi = 90^\circ$; case C: $h = 17cm$, $r = 3cm$, $f = 17cm$, $\alpha_{\max} = 8^\circ$, $h_0 = 8cm$, $\varphi = 90^\circ$; case D: $h = 25cm$, $r = 3cm$, $f = 17cm$, $\alpha_{\max} = 8^\circ$, $h_0 = 8cm$, $\varphi = 90^\circ$; case E: $h = 33cm$, $r = 3cm$, $f = 17cm$, $\alpha_{\max} = 8^\circ$, $h_0 = 8cm$, $\varphi = 90^\circ$.

3.5 Overview of flow patterns

3.5.1 Background

Particle Image Velocimetry (PIV) was used in order to visualize flow patterns and their behavior around harmonically oscillating flexible plate. The goal was to illustrate flow structure close to the surface of the plate and its evolution as a function of plate position within the heave and pitch trajectory.

Harmonically oscillating foil propulsion was and still is a focus of many investigations in the field of hydro- and aerodynamics. Different flow visualization technics have been employed to reveal possible mechanism behind propulsion and ways how to improve it.

In the work of Koochesfahani [40], an airfoil of NACA 0012 type was studied in a pitching motion with small amplitudes around zero angle of attack in water tunnel. With a chord Reynolds number fixed at $12,000$ and for the chosen number of frequencies, flow visualizations and wake velocity measurements were made. The simple motions employed in visualization experiments by Koochesfahani revealed a variety of possible wake structures. At low values of frequencies, below $St = 0.1$, a Kármán vortex street was observed along the trajectory of the trailing edge. With the increase of the frequency, a very different patterns were revealed. For instance, at $St = 0.1$ four vortices per cycle were shed, with two being of the same sign per half cycle. The structure appeared to be very stable for as long as 30 chord lengths downstream. At $St = 0.11$ a rather different pattern emerged. Instead of four, two vortices per cycle were shed, besides that they were arranged in a reverse Kármán street and formed a jet. Further increase of the frequency to $St = 0.14$ caused a respective increase in velocity excess in the jet profile. However, the jet width remained almost unchanged.

Results presented in [40] also revealed strong dependance of wake structure on the kinematics of the foil. By comparing patterns aroused from pitch motions of non sinusoidal type with ones produced by sinusoidal motion, it was observed that asymmetrical wake patterns with multiple vortices were shed per half cycle in the first case. A single strong vortex was created by the fast parts of the cycle, whereas two weaker vortices of the same sign were the result of the slow parts of the cycle. As a result of that, non symmetric motion produced complex wake structures that were not efficient jets.

Buchholz and Smits in [44] performed wake studies and thrust measurements on a series of low-aspect-ratio rectangular pitching panels. Wake structures corresponding to a subset of the thrust measurements were investigated using dye visualization and digital particle image velocimetry. The thrust coefficient was found to be primarily a function of Strouhal number, panel aspect ratio, and Reynolds number, increasing monotonically with each of these parameters. The propulsive efficiency attained a maximum value in the range $0.125 \leqslant St \leqslant 0.34$. The amplitude to span ratio A/S was found to be an important parameter governing both the peak efficiency for a given aspect ratio, and the Strouhal number at which it occurs. At low Strouhal number, the horseshoe vortex shed by the tips and trailing edge of the panel was present in the wake, but as the Strouhal number increased beyond $St = 0.25$ the wake bifurcated into trains of vortex rings connected to the tips of the horseshoes structure, in which two pairs of oppositely signed vortices are shed each pitching cycle. They proposed that the appropriate additional scaling parameter for the effect of three-dimensionality is the ratio of amplitude to span A/S.

The analysis of the influence of wing deformation in locusts on its aerodynamic characteristics was done in [19] by using a three-dimensional computational fluid dynamics simulation based on detailed wing kinematics, and validated against smoke visualizations and digital particle image velocimetry on real locusts. It was shown that wing deformation in locusts is important both in enhancing the efficiency of momentum transfer to the wake and in directing the aerodynamic force vector appropriately for flight.

Leading edge separation and large leading-edge vortices considered a major parameter in the high-lift aerodynamics of insect flight [45], [46]. Alternatively, when high lift is not the major task, attached-flow aerodynamics can offer greater efficiency. The aerodynamic power efficiency of locusts appears to derive from their ability to reduce flow separation and the associated loss of energy as vortical motion in the wake.

In [19] it was suggested that in order for a harmonically oscillating plate to generate high lift with stable leading-edge vortices and to support efficient attached flow aerodynamics, it should undergo appropriate aeroelastic deformation through the course of the wingbeat. Results from CFD simulations demonstrated that time-varying wing twist and camber were essential to the maintenance of attached flow.

3.5.2 A case study for the plate with $1 : 6$ rigid-to-flexible ratio, at $St = 0.26$

In order to illustrate flow patterns near the surface of the plate, the PIV system presented in Section 2.5 was used. Since the possible parameter space for the oscillation plate is large, it was decided to narrow down parameters used in thrust/efficiency experiments, presented earlier, to the transition case where the plate just started to produce thrust and efficiency increased from zero crossing towards its maximum. The value of Strouhal number $St = 0.26$ corresponds to the transition case and the choice of $1 : 6$ rigid-to-flexible ratio plate type was based on its top performance throughout all experiments reported in earlier. Throughout the experiment, the tunnel velocity was kept constant at $U = 0.22m/s$, heave double amplitude h_0 was set to $16cm$, the pitch amplitude θ_0 was set to 16° and the plate was submerged to the middepth of the water tunnel. The experimental survey was divided into several small investigations, each of them intended to illustrate the formation of a particular structure.

In Figures 3.9–3.12, the mean flow is from left to right. Group of Figures 3.9–3.10 corresponds to the downstroke movement, while Figures 3.11–3.12 correspond to the upstroke movement. At the Strouhal number $St = 0.26$, in Figures $3.9(a)-(b)$ one can see that an organized leading edge vortex of a negative sign starts to form on the top side of the plate while the vortex of the positive sign presented on the bottom side of the plate slowly decays as plate upstroke movement stops and downstroke movement begins. Shed trailing edge vortices of the positive sign along with small magnitude vortices of negative sign can be observed as well. Although not shown here, according to [47] and [44] shed vortices are present in the wake for several wavelengths. As the plate begins its downward trajectory, Figure $3.9(b)$, the small leading edge separation vortex of the negative sign starts to grow into larger vortical structure. However, at the bottom side of the plate the positive oriented leading edge vortex travels along the surface of the plate towards the trailing edge.

In Figure $3.10(a)$ one can see that dynamic stall vortex of the positive sign reaches its maximum magnitude, small positive structures of vorticity can be observed within the leading edge vortex, their origin is most likely due to threedimensionality of the problem, the very well observed train of negative oriented structures on the top side of the plate travels towards the trailing edge of the plate and eventually shed into a wake right after the positive vortex from the bottom side of the plate. At the same time positive oriented leading edge vortex continue to travel along the surface of the plate towards the trailing edge.

At the minimum value of heave amplitude, which corresponds to Figure 3.10(b) one can see that the leading edge vortex divided into two substructures, the top one of which was shed along the surface of the plate. This phenomenon was observed previously by Anderson at [47]. It was indicated that while the strong leading edge separation forms, the small secondary leading edge separation can also be observed as the plate stays on its downward trajectory. Eventually the well formed leading edge vortex rolls along the plate and sheds from the trailing edge. This particular process was observed in Figures 3.9–3.10 on the bottom side of the plate, for the positive sign leading edge vortex.

While perfect symmetry does not exist, it is clear from Figures 3.9–3.10 and Figures 3.11–3.12 that downstroke and upstroke movement share a good amount of similarity in terms of the associated flow patterns.

It can be seen on Figures 3.11–3.12 that as the plate moves up along its trajectory, the positive leading edge vortex starts to form on the down side of the plate, while the remains of a leading edge separation structure on the top side continue decay, travel along the surface of the plate and eventually shed into the wake, Figures 3.11$(a)-(b)$. As for the downstroke movement, as the plate approaches its maximum heave position, the dynamic stall vortex forms on the bottom side of the plate Figures 3.11(a). At the same time, a small amount of secondary vorticity forms at this time at the leading edge. Eventually the dynamic stall vortex rolls along the plate Figures 3.11(b), and shed into the wake.

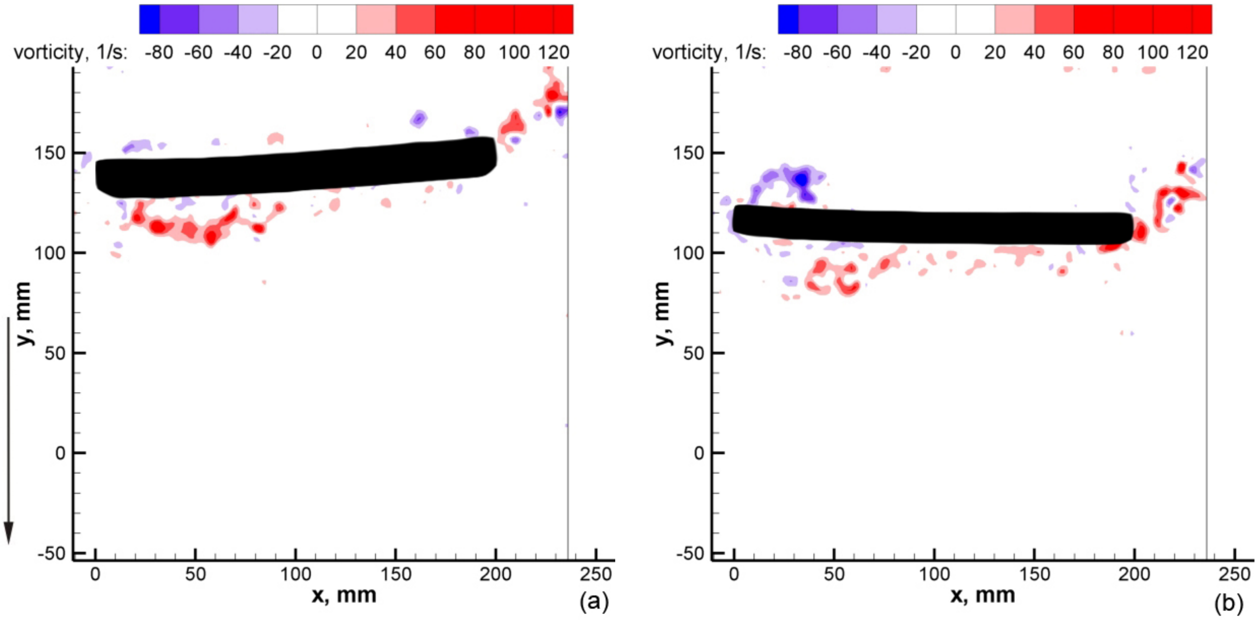

Figure 3.9: PIV vorticity patterns(frames 120 and 227) for the case C for 1 : 6-ratio plate: $h = 17cm$, $r = 3cm$, $f = 17cm$, $\alpha_{\max} = 8^\circ$, $h_0 = 8cm$, $\varphi = 90^\circ$, $St = 0.26$, $f_{osc} = 0.36Hz$, $T = 2.8s$

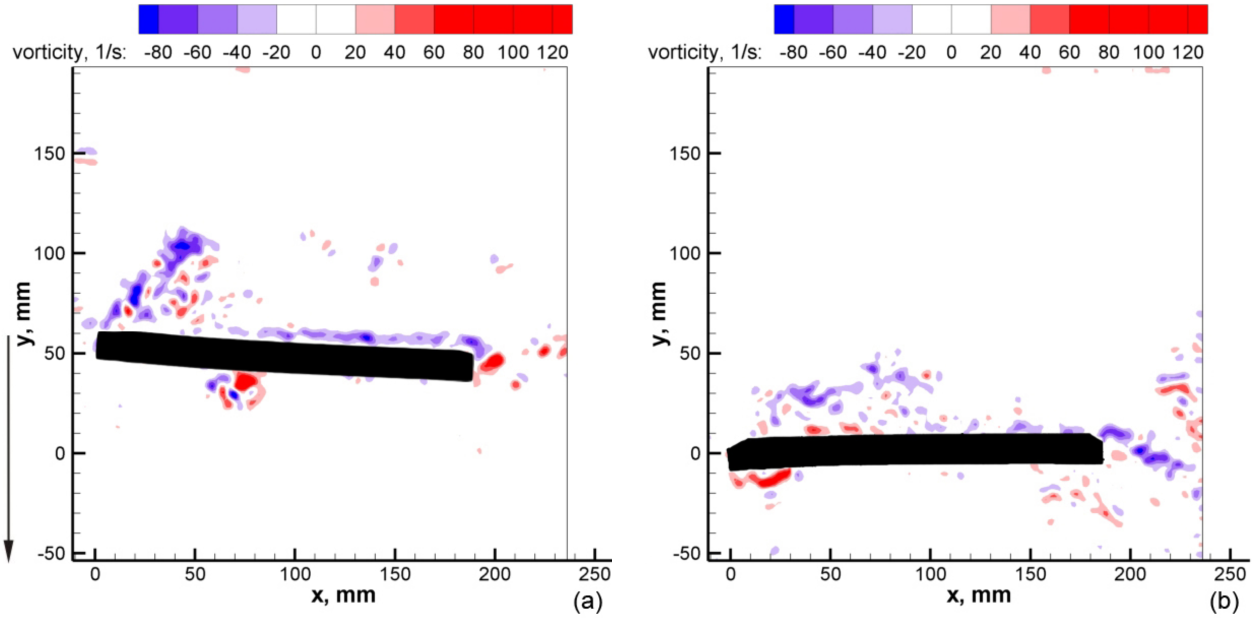

Figure 3.10: PIV vorticity patterns(frames 338 and 389) for the case C for 1 : 6-ratio plate: $h = 17cm$, $r = 3cm$, $f = 17cm$, $\alpha_{\max} = 8^\circ$, $h_0 = 8cm$, $\varphi = 90^\circ$, $St = 0.26$, $f_{osc} = 0.36Hz$, $T = 2.8s$

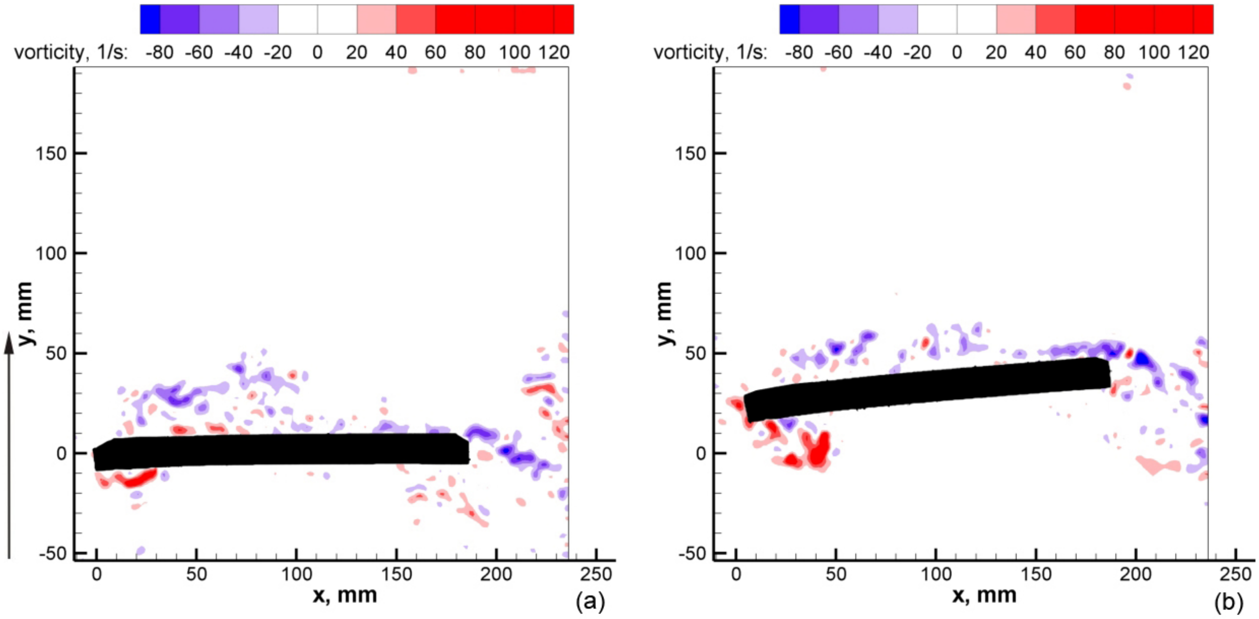

Figure 3.11: PIV vorticity patterns(frames 572 and 656) for the case C for 1 : 6-ratio plate: $h = 17cm$, $r = 3cm$, $f = 17cm$, $\alpha_{\max} = 8°$, $h_0 = 8cm$, $\varphi = 90°$, $St = 0.26$, $f_{osc} = 0.36Hz$, $T = 2.8s$

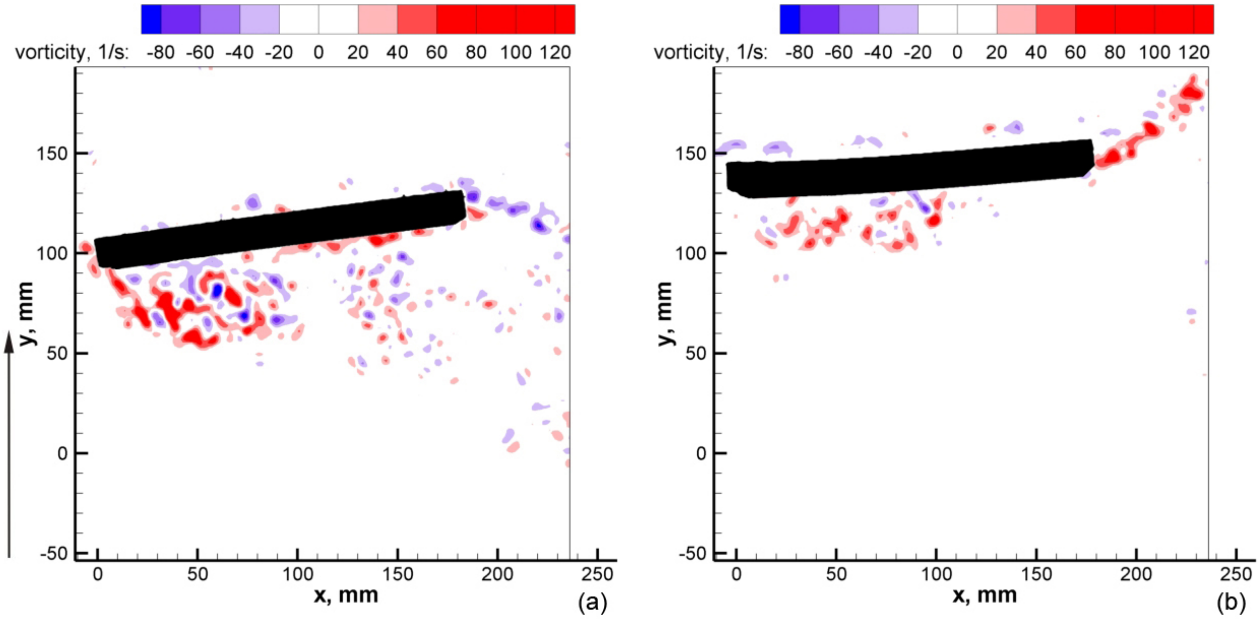

Figure 3.12: PIV vorticity patterns(frames 795 and 960) for the case C for 1 : 6-ratio plate: $h = 17cm$, $r = 3cm$, $f = 17cm$, $\alpha_{\max} = 8°$, $h_0 = 8cm$, $\varphi = 90°$, $St = 0.26$, $f_{osc} = 0.36Hz$, $T = 2.8s$

Chapter 4

Free vibration analysis of Smart Materials

The oscillations of the leading edge of the foil seen in Figure 2.5 have to be accomplished via the tail. Following previous observations, it is believed that matching the natural frequency of the caudal area to the tailbeat frequency improves swimming efficiently. Here, the ability of PZT's to enable frequency adjustments for the caudal area using PZT patches is investigated. The modal influence of the PZT's was studied for the case of a strict A-type velocity feedback law. The sensitivities of the first three modes of vibration to the PZT location and gain magnitude is investigated.

4.1 Eigenproblem formulation

The partial differential equation governing the free vibration of an Euler-Bernoulli beam with viscously distributed damping, is [30]:

$$m(x)\frac{\partial^2}{\partial t^2}w(x,t) + c(x)\frac{\partial}{\partial t}w(x,t) + \frac{\partial^2}{\partial x^2}\left[k(x)\frac{\partial^2}{\partial x^2}w(x,t)\right] = 0. \tag{4.1}$$

The nomenclature developed by Sorrentino et al. [30] is maintained throughout this work and $m(x), c(x), k(x)$ are the mass, damping and stiffness per unit length respectively. In order to investigate the effect of non-proportional viscous damping, the differential equation (4.1) will be considered in a special case when $m(x)$, $c(x)$ and $k(x)$ are piecewise constant across the global domain.

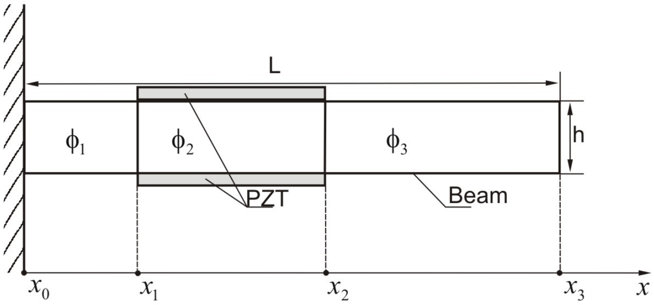

Figure 4.1: Clamped-free EB beam with perfectly bonded piezoelectric actuators.

Assume a solution of equation (4.1) has the form

$$w(x,t) = \phi(x)e^{st}, \tag{4.2}$$

where the generally complex constant s is an eigenvalue of the system that needs to be determined. Substituting equation (4.2) into equation (4.1) gives a differential eigenvalue problem

$$\phi^4 + \sigma\phi = 0, \tag{4.3}$$

with $\sigma = \dfrac{ms^2 + cs}{k}$, and $(\cdot)^4 = \dfrac{d^4}{dx^4}(\cdot)$.

Consider a pair of piezoelectric actuators perfectly bonded to the surface of the beam at x_1 as shown on Figure 4.1. To apply equation (4.3), the beam of Figure 4.1 is segmented into three discrete regions, each with a homogeneous, or a homogenized cross sectional composition. Here, it is shown how the PZT actuators can be represented as an external damping source in the differential eigenvalue problem (4.3).

4.1.1 Segment Solutions

Dividing the beam of length l into 3 segments of length $\Delta x_i = x_i - x_{i-1}$ (where $x_0 = 0$, $x_3 = l$), equation (4.3) reduces to 3 fourth order ordinary differential equations with constant coefficients as follows

$$\phi_i^4(x) = -\sigma_i\phi_i, \quad i = 1, 2, 3 \tag{4.4}$$

with $\sigma_i = \dfrac{m_i s^2 + c_i s}{k_i}$.

Each instance of equation (4.4) reduces to a system of four 1^{st} order ODEs: as an eigenvalue problem.

$$\vec{y_i}' = \mathbf{S}_i \vec{y_i} \tag{4.5}$$

where state vector $\vec{y_i}$ and the companion matrix S_i, specific to the i^{th} segment, are defined as follows $\vec{y_i} = [\phi_i''', \phi_i'', \phi_i', \phi_i]^t$

$$\mathbf{S}_i = \begin{bmatrix} 0 & 0 & 0 & -\sigma_i \\ 1 & 0 & 0 & 0 \\ 0 & 1 & 0 & 0 \\ 0 & 0 & 1 & 0 \end{bmatrix}$$

The four eigenvalues of the companion matrix are $\lambda_{i1} = \sqrt[4]{-\sigma_i} = a_i, \lambda_{i2} = -\sqrt[4]{-\sigma_i} = -a_i, \lambda_{i3} = i\sqrt[4]{-\sigma_i} = ia_i$,
$\lambda_{i4} = -i\sqrt[4]{-\sigma_i} = -ia_i$; so the solution of Eq. (4.4) is

$$\vec{y_i} = \Phi_i e^{\Lambda_i x} \vec{c_i} \tag{4.6}$$

where Φ_i is the ith segment's eigenvector matrix,

$$\Phi_i = \begin{bmatrix} a_i^3 & -a_i^3 & -ia_i^3 & ia_i^3 \\ a_i^2 & a_i^2 & -a_i^2 & -a_i^2 \\ a_i & -a_i & ia_i & -ia_i \\ 1 & 1 & 1 & 1 \end{bmatrix} \tag{4.7}$$

The diagonal matrix Λ_i, contains the ith segment's eigenvalues, $\vec{c_i}$ is the ith segment constant vector. Both Φ_i and Λ_i are elements of $\mathbb{C}^{4\times 4}$.

4.1.2 Interelement Boundary Conditions

Since a segmented beam was considered, continuity across the segment boundary must be enforced by knowledge of internal force, internal moment, slope and displacement changes occurring across each boundary.

At the system boundaries ($x = 0 \quad \& \quad x = l$), any of the common boundary conditions can be written in he form

$$\begin{aligned} B_e \vec{y}_1(0) &= \vec{0}, \\ B_e \vec{y}_N(0) &= \vec{0}. \end{aligned}$$

For example the clamped end and free end shown in Figure 4.1 have the following boundary conditions matrices.

$$B_{e,\text{clamped}} = \begin{pmatrix} 0 & 0 & 1 & 0 \\ 0 & 0 & 0 & 1 \end{pmatrix}, \quad B_{e,\text{free}} = \begin{pmatrix} 1 & 0 & 0 & 0 \\ 0 & 1 & 0 & 0 \end{pmatrix} \tag{4.8}$$

As was mentioned in Section 1.5.1, the piezoelectric actuators can be voltage controlled to generate a shear force on the beam surface that opposes the deformation of the beam. By using the angular velocity feedback (A-type) control [26], the control voltage $V(t)$ is defined as follows:

$$V(t) = K_a(\dot{\Theta}_2 - \dot{\Theta}_1), \tag{4.9}$$

where K_a is the control gain, and $\dot{\Theta}_1 = s\phi_1'(x_1), \dot{\Theta}_2 = s\phi_2'(x_2)$ are the angular velocity values at the left and right ends of the section, as shown on Figure 4.2. The force generated by the PZT element depends on both material and geometric properties of the actuators and is given by the following equation:

$$F_{PZT}(t) = (E_p d_{31} W_p)V(t), \tag{4.10}$$

where $V(t)$ is the applied voltage, d_{31} is the dielectric constant of the actuator, W_p is the width of the PZT element and E_p represents the Young's modulus of the PZT actuator. When bending occurs, the moment induced by the pair of opposing PZT forces is equal to

$$M = t_b F_{PZT} = \Lambda(\dot{\Theta}_2 - \dot{\Theta}_1), \tag{4.11}$$

where $\Lambda = t_b E_p d_{31} W_p K_a$, and t_b is the thickness of the beam to which the PZT actuators are bonded.

To illustrate their action let us consider the section of the beam with two PZT patches attached to its bottom and top sides. Suppose $\dot{\Theta}_1 > \dot{\Theta}_2$, then the beam segment will be bending upwards. In this case piezo-patch needs to produce a moment that tends to bend the beam into a negative curvature profile. As shown in Figure 4.2, the internal bending moment at M_2 is less than the moment at M_1 by value $\Lambda(\dot{\Theta}_2 - \dot{\Theta}_1)$. On the other hand, the moment at M_3 is less than the moment at M_4 by $\Lambda(\dot{\Theta}_2 - \dot{\Theta}_1)$.

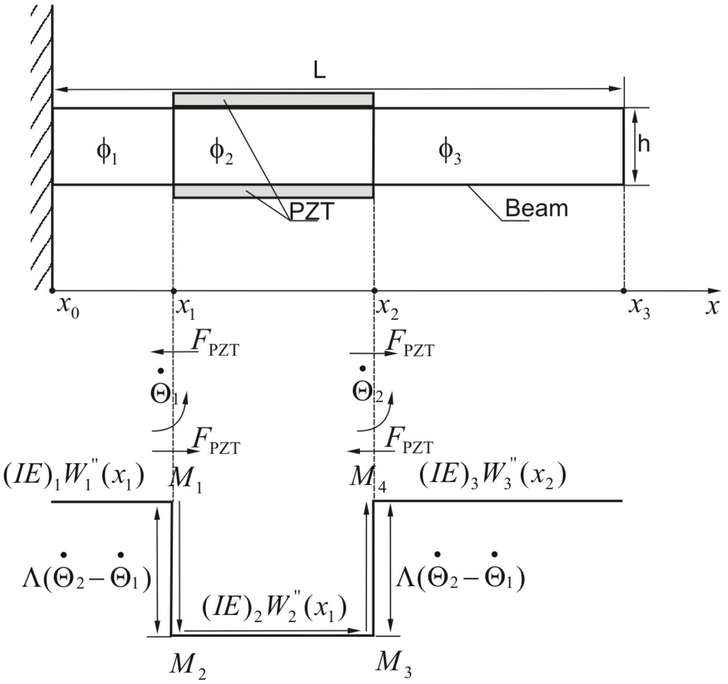

Figure 4.2: Moment diagram of the beam's section with piezoelectric actuators.

Across the first section boundary, the internal force is expected to vary smoothly

$$(EI)_1\phi_1'''(x_1) = (EI)_2\phi_2'''(x_2). \tag{4.12}$$

and the moment balance gives

$$(EI)_1\phi_1''(x_1) = (EI)_2\phi_2''(x_1) + s\Lambda(\phi_2'(x_2) - \phi_1'(x_1)). \tag{4.13}$$

This leads to the following internal conditions at the intermediate point x_1

$$\begin{pmatrix} \phi_2'''(x_1) \\ \phi_2''(x_1) \\ \phi_2'(x_1) \\ \phi_2(x_1) \end{pmatrix} = \begin{pmatrix} \frac{k_1}{k_2} & 0 & 0 & 0 \\ 0 & \frac{k_1}{k_2} & \frac{s\Lambda}{k_2} & 0 \\ 0 & 0 & 1 & 0 \\ 0 & 0 & 0 & 1 \end{pmatrix} \begin{pmatrix} \phi_1'''(x_1) \\ \phi_1''(x_1) \\ \phi_1'(x_1) \\ \phi_1(x_1) \end{pmatrix} + \begin{pmatrix} 0 & 0 & 0 & 0 \\ 0 & 0 & -\frac{s\Lambda}{k_2} & 0 \\ 0 & 0 & 0 & 0 \\ 0 & 0 & 0 & 0 \end{pmatrix} \begin{pmatrix} \phi_2'''(x_2) \\ \phi_2''(x_2) \\ \phi_2'(x_2) \\ \phi_2(x_2) \end{pmatrix} \tag{4.14}$$

where $k_i = (EI)_i$.

Similarly, at the second section boundary x_2, the internal force balance appears as

$$(EI)_2\phi_2'''(x_2) = (EI)_3\phi_3'''(x_3). \tag{4.15}$$

The internal moment balance yields:

$$(EI)_2\phi_2''(x_2) = (EI)_3\phi_3''(x_2) - s\Lambda(\phi_2'(x_2) - \phi_1'(x_1)). \tag{4.16}$$

This leads to the interelement boundary conditions at location x_3 in the following form

$$\begin{pmatrix} \phi_2'''(x_2) \\ \phi_2''(x_2) \\ \phi_2'(x_2) \\ \phi_2(x_2) \end{pmatrix} = \begin{pmatrix} \frac{k_2}{k_3} & 0 & 0 & 0 \\ 0 & \frac{k_2}{k_3} & \frac{s\Lambda}{k_3} & 0 \\ 0 & 0 & 1 & 0 \\ 0 & 0 & 0 & 1 \end{pmatrix} \begin{pmatrix} \phi_2'''(x_2) \\ \phi_2''(x_2) \\ \phi_2'(x_2) \\ \phi_2(x_2) \end{pmatrix} + \begin{pmatrix} 0 & 0 & 0 & 0 \\ 0 & 0 & -\frac{s\Lambda}{k_3} & 0 \\ 0 & 0 & 0 & 0 \\ 0 & 0 & 0 & 0 \end{pmatrix} \begin{pmatrix} \phi_1'''(x_1) \\ \phi_1''(x_1) \\ \phi_1'(x_1) \\ \phi_1(x_1) \end{pmatrix} \tag{4.17}$$

To follow the conventional recursive process of the transfer matrix approach used by Sorrentino[30], it is necessary for equations (4.14) and (4.17) to appear as

$$\vec{y}_i(x_{i-1}) = \mathbf{A}_{i-1}\vec{y}_{i-1}(x_{i-1}). \tag{4.18}$$

Let

$$\mathbf{B}_{11} = \begin{pmatrix} \frac{k_1}{k_2} & 0 & 0 & 0 \\ 0 & \frac{k_1}{k_2} & \frac{s\Lambda}{k_2} & 0 \\ 0 & 0 & 1 & 0 \\ 0 & 0 & 0 & 1 \end{pmatrix}, \quad \mathbf{B}_{12} = \begin{pmatrix} 0 & 0 & 0 & 0 \\ 0 & 0 & -\frac{s\Lambda}{k_2} & 0 \\ 0 & 0 & 0 & 0 \\ 0 & 0 & 0 & 0 \end{pmatrix} \tag{4.19}$$

$$\mathbf{B}_{21} = \begin{pmatrix} 0 & 0 & 0 & 0 \\ 0 & 0 & -\frac{s\Lambda}{k_2} & 0 \\ 0 & 0 & 0 & 0 \\ 0 & 0 & 0 & 0 \end{pmatrix}, \quad \mathbf{B}_{22} = \begin{pmatrix} \frac{k_1}{k_2} & 0 & 0 & 0 \\ 0 & \frac{k_1}{k_2} & \frac{s\Lambda}{k_2} & 0 \\ 0 & 0 & 1 & 0 \\ 0 & 0 & 0 & 1 \end{pmatrix}, \tag{4.20}$$

where the first subscript refers to the node number being considered and the second subscript refers to the position dependence. With this notations, for instance, B_{22} refers to a matrix in the internal force/moment balance at node 2 and defines a contribution due to the state at node 2.

The set of boundary conditions, equations 4.14 and 4.17 can be rewritten as follows

PZT Boundaries: at x_1 and x_2 accordingly

$$\vec{y}_2(x_1) = \mathbf{B}_{11}\vec{y}_1(x_1) + \mathbf{B}_{12}\vec{y}_2(x_2), \tag{4.21}$$

$$\vec{y}_3(x_2) = \mathbf{B}_{22}\vec{y}_2(x_2) + \mathbf{B}_{21}\vec{y}_2(x_1). \tag{4.22}$$

The global boundary conditions are

Wall Boundary:

$$B_{e,\text{clamped}}\vec{y}_1(x_0) = \vec{0}. \tag{4.23}$$

Free End Boundary:

$$B_{e,\text{free}}\vec{y}_3(x_3) = \vec{0}, \tag{4.24}$$

where $B_{e,\text{clamped}}$ and $B_{e,\text{free}}$ are defined in (4.8).

4.1.3 Recursive procedure

Given the shape of the i^{th} segment from (4.6), and supposing that $\vec{y}_i(x_{i-1})$ is known, then following [30]:

$$\vec{y}_i(x_{i-1}) = \Phi_i e^{\Lambda_i x_{i-1}}\vec{c}_i \tag{4.25}$$

which gives $\vec{c}_i = e^{-\Lambda_i x_{i-1}}\Phi_i^{-1}\vec{y}_i(x_{i-1})$. This allows equation (4.6) to be rewritten as

$$\vec{y}_i(x) = \Phi_i e^{\Lambda_i(x-x_{i-1})}\Phi_i^{-1}\vec{y}_i(x_{i-1}). \tag{4.26}$$

Thus, the mode shapes on each of three segments are given by the following expressions

$$\vec{y}_1(x_1) = \Phi_1 e^{\Lambda_1(x_1-x_0)}\Phi_1^{-1}\vec{y}_1(x_0), \tag{4.27}$$

$$\vec{y}_2(x_2) = \Phi_2 e^{\Lambda_2(x_2-x_1)}\Phi_2^{-1}\vec{y}_2(x_1), \tag{4.28}$$

$$\vec{y}_3(x_3) = \Phi_3 e^{\Lambda_3(x_3-x_2)}\Phi_3^{-1}\vec{y}_3(x_2). \tag{4.29}$$

Equations (4.27)–(4.29) will be used in the expressions for interelement constraint equations (4.21) and (4.22) to generate a recursive equation of the form of equation (4.18).

For equation (4.21) this yields,

$$\begin{aligned}
\vec{y}_2(x_1) &= \mathbf{B}_{11}\vec{y}_1(x_1) + \mathbf{B}_{12}\{\Phi_2 e^{\Lambda_2(x_2-x_1)}\Phi_2^{-1}\}\vec{y}_2(x_1),\\
\vec{y}_2(x_1) &= \left[\mathbf{I} - \mathbf{B}_{12}\Phi_2 e^{\Lambda_2(x_2-x_1)}\Phi_2^{-1}\right]^{-1}\mathbf{B}_{11}\vec{y}_1(x_1),\\
\vec{y}_2(x_1) &= \mathbf{B}_{12}^{*}{}^{-1}\mathbf{B}_{11}\vec{y}_1(x_1),
\end{aligned}$$

where $\mathbf{B}_{12}^{*} = \mathbf{I} - \mathbf{B}_{12}\Phi_2 e^{\Lambda_2(x_2-x_1)}\Phi_2^{-1}$. Hence

$$\vec{y}_2(x_1) = \mathbf{A}_1\vec{y}_1(x_1), \tag{4.30}$$

where $\mathbf{A}_1 = \mathbf{B}_{12}^{*}{}^{-1}\mathbf{B}_{12}$.

Similarly, equation (4.22) can be rewritten as follows

$$\begin{aligned}
\vec{y}_3(x_2) &= \mathbf{B}_{22}\vec{y}_2(x_2) + \mathbf{B}_{21}\{\Phi_2 e^{-\Lambda_2(x_2-x_1)}\Phi_2^{-1}\}\vec{y}_2(x_2),\\
\vec{y}_3(x_2) &= \left[\mathbf{B}_{22} + \mathbf{B}_{21}\Phi_2 e^{-\Lambda_2(x_2-x_1)}\Phi_2^{-1}\right]\vec{y}_2(x_2).
\end{aligned}$$

It follows that

$$\vec{y}_3(x_2) = \mathbf{A}_2\vec{y}_2(x_2), \tag{4.31}$$

where $\mathbf{A}_2 = \mathbf{B}_{22} + \mathbf{B}_{21}\Phi_2 e^{-\Lambda_2(x_2-x_1)}\Phi_2^{-1}$.

By combining equations (4.26),(4.30) and (4.31), one can obtain

$$\vec{y}_3(x_3) = \left[\Phi_3 e^{\Lambda_3(x_3-x_2)}\Phi_3^{-1}\mathbf{A}_2\right]\left[\Phi_2 e^{\Lambda_2(x_2-x_1)}\Phi_2^{-1}\mathbf{A}_1\right]\left[\Phi_1 e^{\Lambda_1(x_1-x_0)}\Phi_1^{-1}\right]\vec{y}_1(0), \tag{4.32}$$

which makes it possible to express $\vec{y}(l)$ as a function of $\vec{y}(0)$. That is,

$$\vec{y}_3(l) = \Pi_3(l)\vec{y}_1(0) \tag{4.33}$$

Applying equation (4.33) to the boundary condition yields:

$$\begin{cases}
\mathbf{B}_0\Phi_1\vec{c}_1 &= \vec{0},\\
\mathbf{B}_3\Pi_3(l)\Phi_1\vec{c}_1 &= \vec{0}.
\end{cases}$$

These boundary conditions form a set of four linear homogeneous algebraic equations in four unknowns $c_1(i)$ and can be rewritten as follows

$$\Theta\vec{c}_1 = 0. \tag{4.34}$$

	Beam	**PZT actuators**
Material	Stainless Steel	Lead Zirconium Titanate
Modulus	$193 \times 10^9\ N/m^2$	$63 \times 10^9\ N/m^2$
Length	$1\ m$	$0.05\ m$
Thickness	$0.000381\ m$	$0.000254\ m$
Width	$0.03202\ m$	$0.020574\ m$
Density	$8000\ kg/m^3$	$7600\ kg/m^3$
d_{31}	n/a	$179 \times 10^{-12}\ m/V$

Table 4.1: System parameters.

Recalling that the elements of matrix Θ depend on the unknown eigenvalue s, and that Eq.(4.34) admits non-trivial solution if and only if the determinant of the coefficient matrix is zero, then solution of

$$det[\Theta] = 0 \tag{4.35}$$

provides the desired eigenvalues of the differential eigenvalue problem given by equation(4.5).

4.2 Eigenproblem solution

The solution procedure that will be presented in the following sections has two stages. First, calculation of the frequency and second, the evaluation of the mode shapes. The important inputs to the analysis of the frequencies and mode shapes are the location x_1 of the PZT patch along the surface of the beam, and the control gain value K_a. By varying those parameters it was possible to establish the PZT effectiveness.

Figure 4.3 shows a cross section view of the PZT laminated beam considered in this work with system parameters presented in Table 4.1. The two pieces of PZT elements are made of lead zirconium titanate ($E_{PZT} = 63 \times 10^9 N/m^2$) and the beam is made of stainless steel ($E_{BEAM} = 193 \times 10^9 N/m^2$). The homogenized section exhibits an equivalent bending stiffness, is made entirely of stainless steel, and is also shown in Figure 4.3. The homogenization method assumes that PZT surface bond is perfect and that the laminated beam section is in pure bending. Since

$$n = \frac{E_{PZT}}{E_{BEAM}} = \frac{63 \times 10^9 N/m^2}{193 \times 10^9 N/m^2} = 0.326$$

the width of the top and bottom portion of steel, which replaces the original PZT

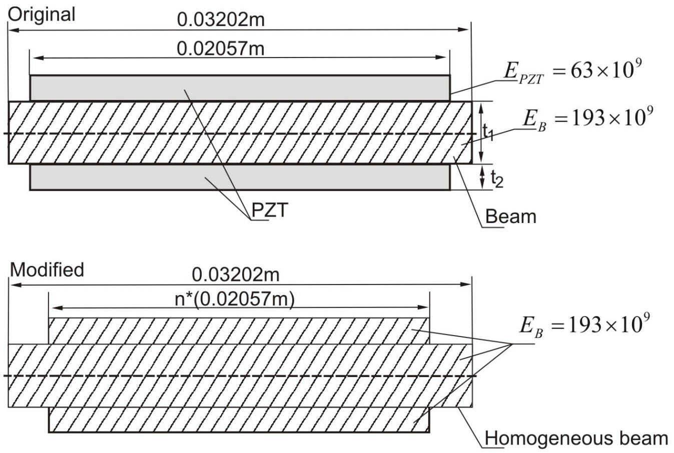

Figure 4.3: Original and transformed section of the composite middle part of the beam.

material, is obtained by multiplying the original width by 0.326. This change in dimension occurs in a direction parallel to neutral axis. The moment of inertia of the transformed section about its centroidal axis is

$$I = \frac{1}{12}b_1 t_1^3 + 2\left[\frac{1}{12}b_2 t_2^3 + \frac{b_2 t_2}{4}(t_1 + t_2)^2\right] \tag{4.36}$$

Hence, by using expression (4.36) one can evaluate coefficients $k_i = I_i E_i$ on each of the three sections of the beam. The computation of the mode shapes has two stages, outlined below.

4.2.1 Eigenvalues

Equation (4.35) needs to be solved numerically in order to find the first eigenvalues s_j, s_j^* of the differential eigenvalue problem (4.3). It is necessary to mention that s_j^* is a remnant of the solution process, has no physical bearing on the beam vibration, and can be eliminated from consideration.

A zero finding routine based on the secant method was used as described in [48]. In order to apply that routine, one needs to have an initial approximation that eventually should converge to the desired eigenvalue. Rayleigh's method [49] was applied to find an upper bound on the fundamental frequency of the PZT laminated beam for each PZT location. For the sectioned beam, shown in Figure 4.2 the natural frequencies can be found from the following expression

$$\omega_i^2 = \frac{E_1 I_1 \int_0^{x_1} \left(\frac{d^2 W_i}{dx^2}\right)^2 dx + E_2 I_2 \int_{x_1}^{x_2} \left(\frac{d^2 W_i}{dx^2}\right)^2 dx + E_3 I_3 \int_{x_2}^{x_3} \left(\frac{d^2 W_i}{dx^2}\right)^2 dx}{\rho A_1 \int_0^{x_1} W_i^2 dx + \rho A_2 \int_{x_1}^{x_2} W_i^2 dx + \rho A_3 \int_{x_2}^{x_3} W_i^2 dx}. \tag{4.37}$$

Here $W_i(x)$ is approximated as the i-th normal mode of the beam without any PZT attached. In addition, $I_3 = I_1 = I_{BEAM}$, $E_1 = E_2 = E_3 = E_{BEAM}$ and $I_2 = I_{BEAM+PZT}$ obtained from expression (4.36).

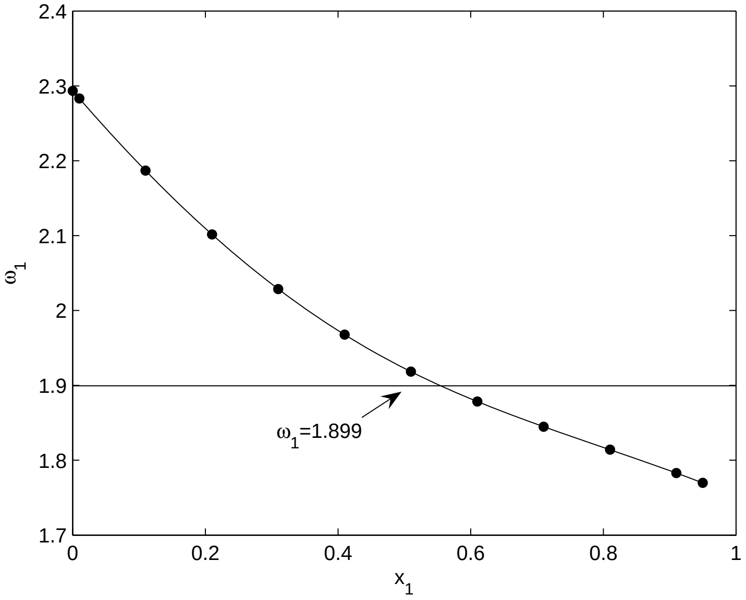

Figure 4.4: Fundamental frequency ω_1 of the beam as a functions of leading edge position x_1.

Plots for the first, second and third fundamental frequencies as a function of PZT location are presented in the Figures 4.4-4.6, where the effect of the added PZT material, simulated by adding the PZT with $K_a = 0$, can be observed. On each plot, the corresponding value of the original natural frequency $\omega_i, \quad i = 1, 2, 3$ is presented as a horizontal line, for comparison. As seen in Figures 4.4-4.6 only limited portions of the curves lie below the original ω_i values. Referring to equation (4.37), the increased value of I_2 overcompensates the addition of the PZT mass, leading to an increase in beam natural frequency for most PZT placements.

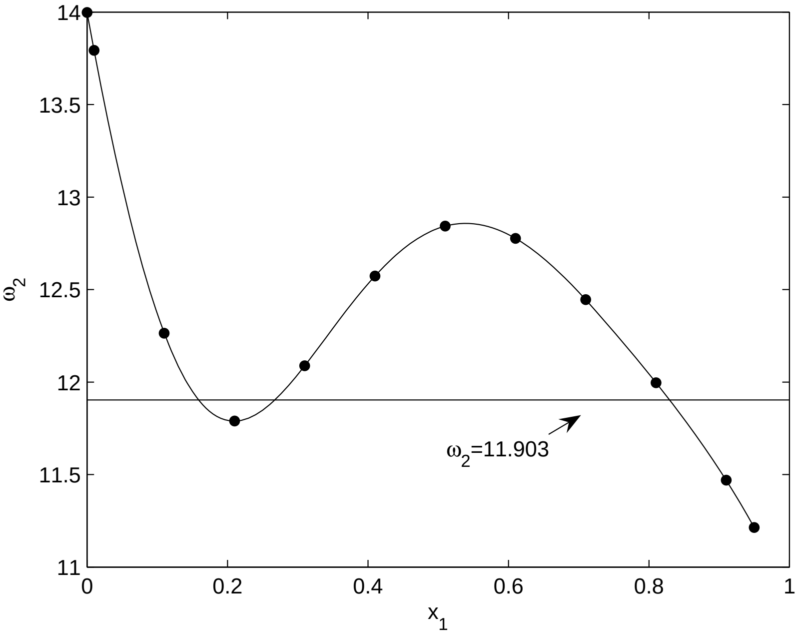

Figure 4.5: Fundamental frequency ω_2 of the beam as a functions of PZT leading edge position x_1.

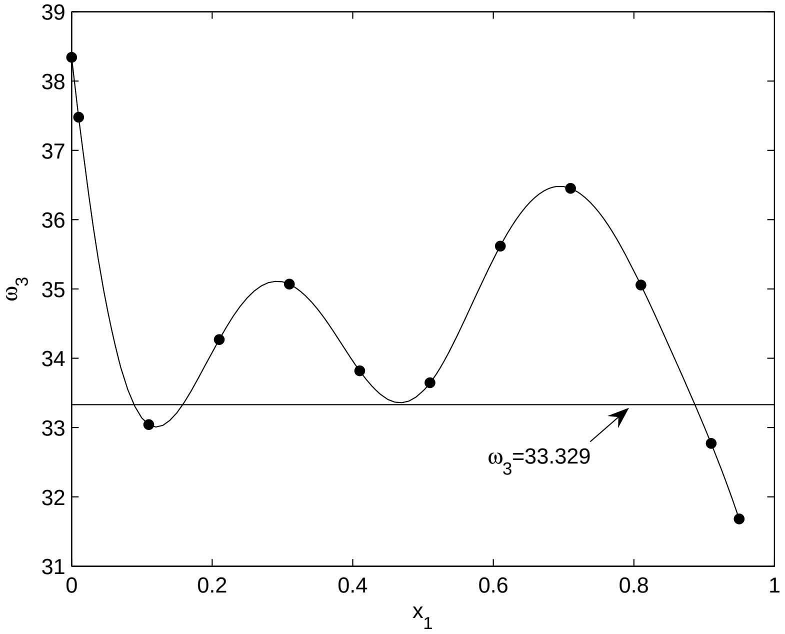

Figure 4.6: Fundamental frequency ω_3 of the beam as a functions of PZT leading edge position x_1.

4.2.2 Eigenfunctions

The procedure of finding mode shapes can be described as follows. For each s_j where $j = 1, 2, 3$ one must solve Eq.(4.34) to find $\vec{c_1}^{(j)}$. By looking at Eq.(4.34) it is easy to observe that $\vec{c_1}^{(j)}$ is an eigenvector of Θ that corresponds to zero eigenvalue of Θ.

Once the $\vec{c_1}^{(j)}$ are known, equation (4.6) with $i = 1, 2, 3$ is used to obtain portions of the modeshape on each of three segments. That is, $\vec{y_1}(x), \vec{y_2}(x), \vec{y_3}(x)$:

$$\vec{y_1}(x) = \Phi_1 e^{\Lambda_1 (x - x_0)} \Phi_1^{-1} \vec{y_1}(x_0), x \in (0, x_1) \tag{4.38}$$

$$\vec{y_2}(x) = \Phi_2 e^{\Lambda_2 (x - x_1)} \Phi_2^{-1} \vec{y_2}(x_1), x \in (x_1, x_2) \tag{4.39}$$

$$\vec{y_3}(x) = \Phi_3 e^{\Lambda_3 (x - x_2)} \Phi_3^{-1} \vec{y_3}(x_2), x \in (x_2, x_3). \tag{4.40}$$

Chapter 5

Comments, results and discussion on the design of flexible propulsors.

In Figure 5.1, the loci for the first three eigenvalues s_1, s_2, s_3 of the PZT laminated beam are shown. The plots illustrate how the location x_1 and gain K_a create changes in s_j, $j = 1, 2, 3$. In Figure 5.1, each curve corresponds to a particular PZT location, defined by x_1. For $K_a = 0$, the curve intersects the imaginary axis and $Im\{s_j\}$ is minimal. As K_a increases, the value of s_j traces out an elliptical curve. It can be seen in Figure 5.1 that, for the beam geometry and material considered, and for the case of a single PZT actuator, the A-type control influences the higher modes much more then the first mode of vibration. The detailed discussion regarding each of the first three modes is presented in the following sections.

The uncontrolled modes exhibit identically zero real parts, and as K_a is increased the real part of s_1, s_2, and s_3 reaches a local minima. Further increase in K_a results in a reduced vibration dissipation tendency, and the complex values of s_1, s_2, s_3 return towards the imaginary axis, as the gain K_a approaches infinity. It should be noted that as $K_a \to \infty$, $Im\{s_j\}$ approaches a magnitude corresponding to the natural frequency of the PZT laminated beam section, located between x_1 and x_2, with clamped-clamped boundary conditions. Note that the A-type control never produces instability even as $K_a \to \infty$. This is in agreement with the stability conditions presented by Sun at al. in [50].

Referring to the motivation of this work, there are two aspects of the PZT effect that are of interest: the induced changes in vibration frequency and the vibration suppression characteristic. The potential for modifying the natural frequency of a caudal area of the fish tail to align it with the tailbeat frequency is best judged by the vertical spread of each elliptical loci.

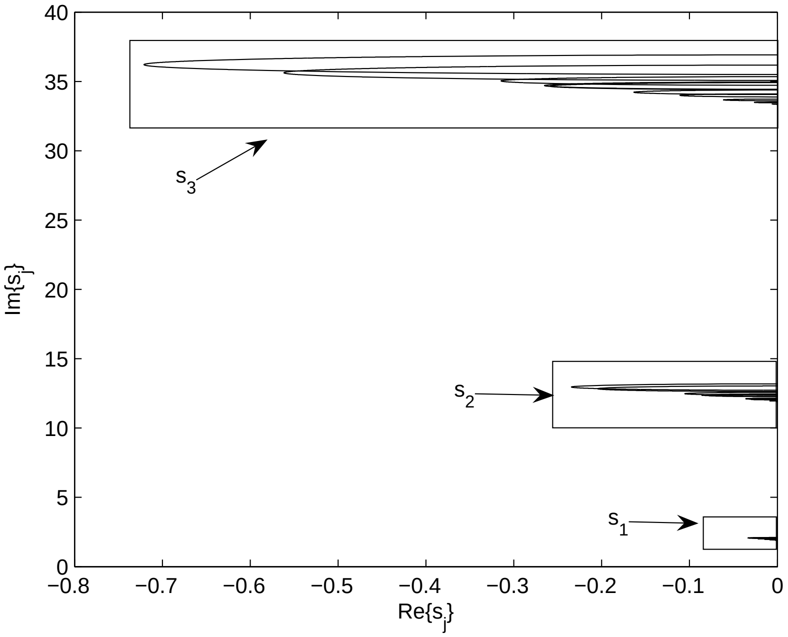

Figure 5.1: Root-locus of complex natural frequencies s_1, s_2, s_3 obtained for 12 different positions of the PZT patches and with increasing damping coefficients.

If the PZT patch is to be used to suppress "caudal area" oscillations and preserve a specific shape, the transient vibration response induced by propulsive oscillations in the preceding moments needs to be suppressed. The suppression is best judged by the horizontal spread of each elliptical loci. Maximum vibration suppression occurs when the real part of the eigenvalue is minimized.

5.1 Frequency shifting and vibration suppression

Figures 5.2-5.4 show root-locus diagrams for the first three modes of the PZT laminated beam and provide some insight into the changing behavior of the flexible beam due to the incremental changes in the control gain K_a and the position of the PZT actuator. The individual curves correspond to a particular value of x_1, the location of the PZT patch leading edge. Each individual curve starts when $K_a = 0$, and ends when the eigenvalue is within 10^{-8} of the imaginary axis.

On all three plots it can be seen that frequency always increases with increasing

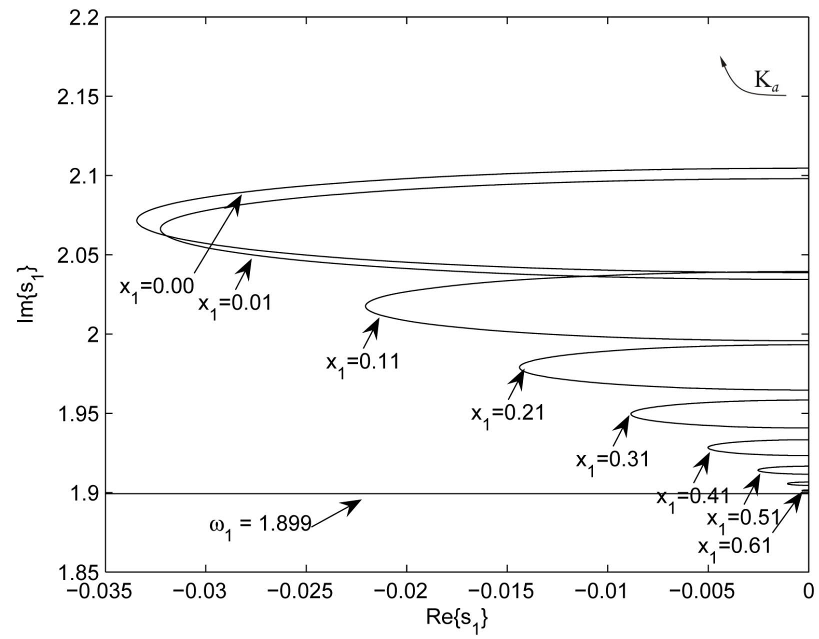

Figure 5.2: Root-locus of complex natural frequency s_1 obtained for 12 different positions of the PZT patches and with increasing damping coefficients.

K_a values. The lower bound of the adjusted mode frequency is controlled by the position of the PZT patch on the beam surface. When the PZT is added near an antinode of the original normal mode, the lower bound is dropped significantly. In general for all modes, as the PZT is positioned to lower the vibration frequency, the PZT's effects on vibration frequency and suppression are attenuated.

The sensitivity of the first mode to K_a and x_1 is presented in Figure 5.2. As one slides the PZT patch along the beam, the overall change in s_1 seen across the full range of K_a values is negligible. If $x_1 \geqslant 0.61m$ the reduction in the PZT effect is small resulting in ineffectiveness of the PZT in this position. Figure 5.2 shows that the best placement for the PZT patch to enable and disable the increased stiffness and vibration suppression at the fixed end. This observation agrees with placement suggestion presented in [31].

The PZT effect on the second mode is presented by the root-locus diagram of Figure 5.3. As with the first mode shown in Figure 5.2, the larger the maximum $|Re\{s_j\}|$ for a given PZT location, the greater is the range of $Im\{s_j\}$ produced by changing K_a. That is, the suppression and frequency modulation tasks are complementary with respect to PZT location. However, Figure 5.3 shows that the attenuation of the

PZT effects observed as the PZT was moved towards the free end is not replicated for the second mode. Rather $0.11 \leqslant x_1 \leqslant 0.31$ and $x_1 \geqslant 0.71$ are locations which yield a negligible PZT effect. At the root of the beam, and in between these regions, the PZT actuators can significantly influence the beam vibration.

Another noticeable difference between the cases presented in Figures 5.2 and 5.3 is the range of attainable $Re\{s_j\}$ values for $j = 1, 2$. The range of real values covered in Figure 5.3 is 10 times larger than that of Figure 5.2. Placement of the PZT patch near the root of the beam still shows the best influence on the vibration frequency and the vibration suppression characteristics.

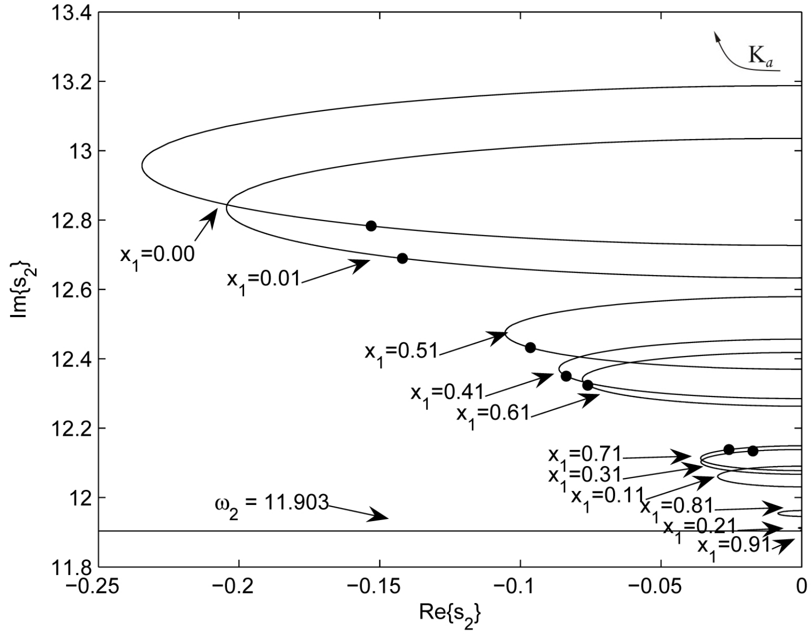

Figure 5.3: Root-locus of complex natural frequency s_2 obtained for 12 different positions of the PZT patches and with increasing damping coefficients.

The PZT effects on the third mode is presented in Figure 5.4. As in Figure 5.3, the root-locus diagrams for different PZT locations are separated into well distinguished groups: $x = [0.00m, 0.01m]$, $x = [0.71m, 0.61m, 0.31m]$, $x = [0.21m, 0.81m]$ and $x = [0.41m, 0.51m, 0.91m, 0.11m]$. As for the second mode, the root-locus for $x_1 = 0.95$ is not visible on the graphs as PZT effect is negligible at this location. Note that this is logical since there is no curvature at the free end. Thus the difference $(\dot{\Theta}_2 - \dot{\Theta}_1)$, and the PZT voltage that depends on it, should be very small at the end. Considering the third mode $x_1 = 0.11, 0.21m, 0.41m, 0.51m, 0.81m - 0.95$ are not suitable placements,

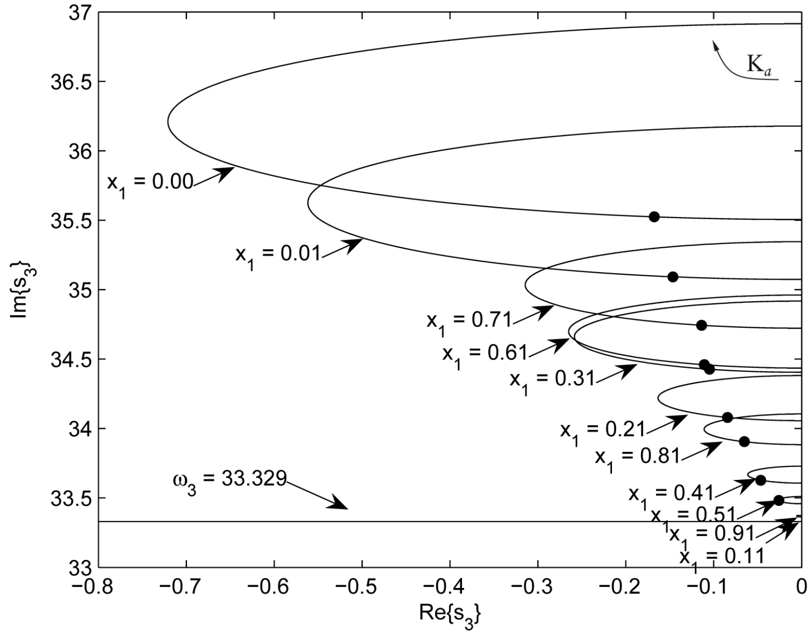

Figure 5.4: Root-locus of complex natural frequency s_3 obtained for 12 different positions of the PZT patches and with increasing damping coefficients.

as the PZT effectiveness at those locations is negligible.

The range of possible $Re\{s_3\}$ values in Figure 5.4 is almost 4 times greater than that of the second mode shown in Figure 5.3. Similar to modes one and two, placement at the root of the beam maximizes PZT patch's suppression and frequency shifting abilities.

5.2 Saturation Constants

The curves in Figures 5.2 – 5.2 are not bounded by the physical limits of the PZT material. It is important to note that increasing K_a values lead to increases in the voltage supplied to the PZT actuators. However, the PZT actuators are subject to a supplied saturation voltage which should not be exceeded.

For the PZT elements considered in the present study, the saturation voltage is $200V$. With PZT saturation in mind, the curves of Figures 5.2 – 5.4 need to be bounded by considering a characteristic amplitude of the free vibrations considered, and the voltages produced by the A-type feedback law for this amplitude. Mode shapes obtained from equations (4.38) – (4.40) were normalized to ensure that the maximum deflection across the beam was $0.1L$.

The choice of a scaling factor for a mode shape represented by a complex valued function was a challenge. For a single PZT patch, the overall mode shape is a piecewise smooth function that consists of three parts. The procedure involved in finding maximum of this complex function for each of three segments of the mode shape function. Then, the overall maximum value, denoted by $maxfactor$, was determined. Finally, each mode shape was multiplied by a factor $0.1/maxfactor$. This normalization procedure was necessary to account for the asynchronous nature of the modes; one has to locate the instant of maximum displacement which is not always demonstrated within the real-valued projection of the mode shapes. Once mode shapes were scaled, the applied voltage can be determined from equation (4.9).

The following Tables 5.1 and 5.2 present s_j, $(j = 1, 2, 3)$ values corresponding to the PZT actuators reaching their saturation voltage limit along with respective values of the gain constant K_a. These saturation K_a values are plotted as dots on corresponding locus curves in Figure 5.3 – 5.4. For mode one, the voltage did not reach its saturation limit for any of the PZT locations considered.

It can be seen in Table 5.1 that the saturation voltage limit is reached substantially earlier than the $Re\{s_2\}$ minima presented in Figure 5.3 are achieved. However, the saturation points indicated are specific to the amplitude of vibration, $0.1L$, considered. If small scale vibrations are ensured, larger gains could be accommodated. Even including saturation constraints, the PZT positions near the beam root, such as $x_1 = 0.00$ and $x_1 = 0.01$, still produce the maximum vibration suppression. From Table 5.1 one can see that minimal $Re\{s_2\}$ values at these points are very close to each other, and hence these locations have almost identical influence on the second mode when saturation is considered. A similar observation can be made for the third mode.

The results introduced in Figures 5.2 – 5.4 and Tables 5.1 – 5.2 lead one to conclude that for the clamped-free beam, the most effective PZT position is the one located near the fixed end. Both root-locus plots and saturation voltage analysis support this result.

Table 5.1: Eigenvalues s_2 rad/s corresponding to the PZT actuators reaching their saturation voltage limit $200V$ along with respective values of the gain constant K_a

PZT location	Eigenvalue, s_2	Voltage	Gain, K_a
$x_1 = 0.00$	$-0.153 + 12.782i$	$200V$	1311
$x_1 = 0.01$	$-0.141 + 12.689i$	$200V$	1339
$x_1 = 0.11$	Whole loop	N/A	N/A
$x_1 = 0.21$	Whole loop	N/A	N/A
$x_1 = 0.31$	$-0.017 + 12.134i$	$200V$	2022
$x_1 = 0.41$	$-0.084 + 12.350i$	$200V$	1632
$x_1 = 0.51$	$-0.096 + 12.432i$	$200V$	1521
$x_1 = 0.61$	$-0.076 + 12.323i$	$200V$	1639
$x_1 = 0.71$	$-0.025 + 12.138i$	$200V$	2009
$x_1 = 0.81$	Whole loop	N/A	N/A
$x_1 = 0.91$	Whole loop	N/A	N/A
$x_1 = 0.95$	Whole loop	N/A	N/A

Table 5.2: Eigenvalues s_3 rad/s corresponding to the PZT actuators reaching their saturation voltage limit $200V$ along with respective values of the gain constant K_a

PZT location	Eigenvalue, s_3	Voltage	Gain, K_a
$x_1 = 0.00$	$-0.168 + 35.524i$	$200V$	1029
$x_1 = 0.01$	$-0.146 + 35.093i$	$200V$	1034
$x_1 = 0.11$	Whole loop	N/A	N/A
$x_1 = 0.21$	$-0.084 + 34.080i$	$200V$	1073
$x_1 = 0.31$	$-0.105 + 34.427i$	$200V$	1054
$x_1 = 0.41$	$-0.046 + 33.628i$	$200V$	1130
$x_1 = 0.51$	$-0.026 + 33.482i$	$200V$	1272
$x_1 = 0.61$	$-0.111 + 34.459i$	$200V$	1056
$x_1 = 0.71$	$-0.114 + 34.743i$	$200V$	1045
$x_1 = 0.81$	$-0.065 + 33.905i$	$200V$	1084
$x_1 = 0.91$	Whole loop	N/A	N/A
$x_1 = 0.95$	Whole loop	N/A	N/A

5.3 Mode Shapes

In Figures 5.5, 5.6, and 5.6 the mode shapes for the first three modes, before the saturation limit was reached are shown. The mode shapes correspond to 40 equally spaced K_a values for each of the PZT locations considered in Figures 5.2 – 5.4.

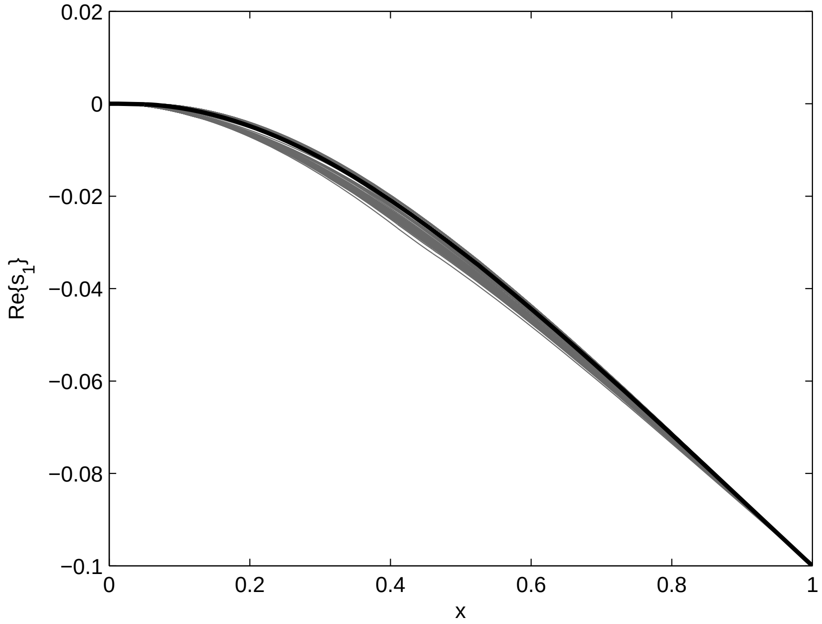

Figure 5.5: Envelope of the first mode shapes obtained at each of the 12 PZT locations considered in this study.

In general, the mode shapes are more sensitive to x_1 then K_a. However, for some locations, K_a adjustments can significantly affect the shape. The curves in Figures 5.6 – 5.9 illustrate how the saturation limit effect the mode shapes when the PZT patch is placed at an inflection point. In all plots, the thick black curve represents the undamped mode shape. It can be seen that when $x_1 = 0.41$ for the second mode, and $x_1 = 0.31$ for the third mode, changes in K_a produce drastic mode shape changes. It is also evident that the non-proportional damping effect imposed by the PZT elements is more acute for the higher order modes. This observation agrees with those in [30].

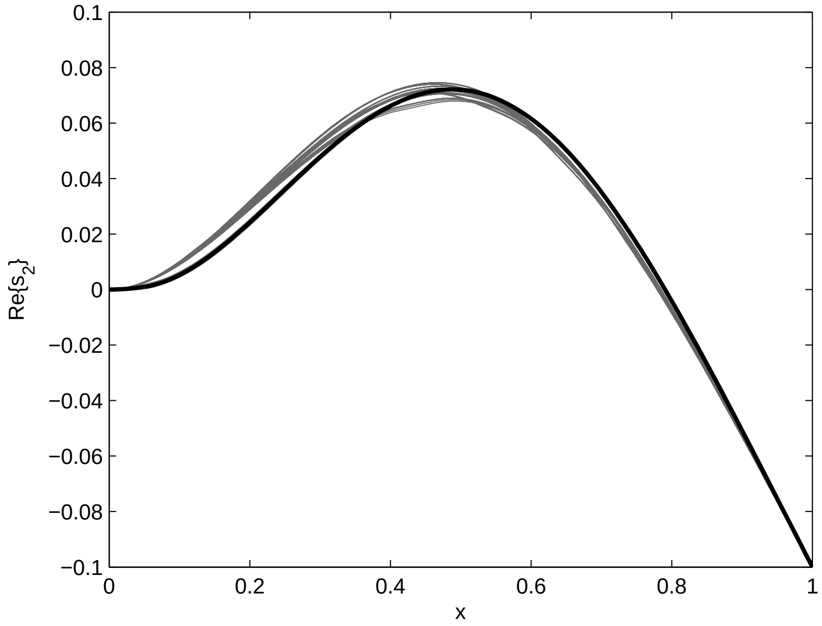

Figure 5.6: Envelope of the second mode shapes obtained at 12 PZT locations considered in this study, before saturation limit.

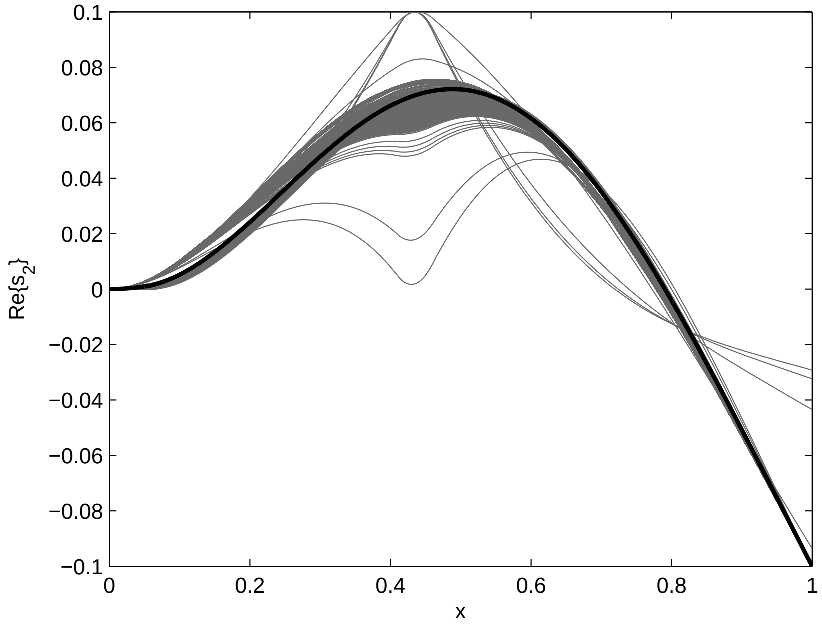

Figure 5.7: Envelope of the second mode shapes obtained at 12 PZT locations considered in this study, no saturation constraints considered.

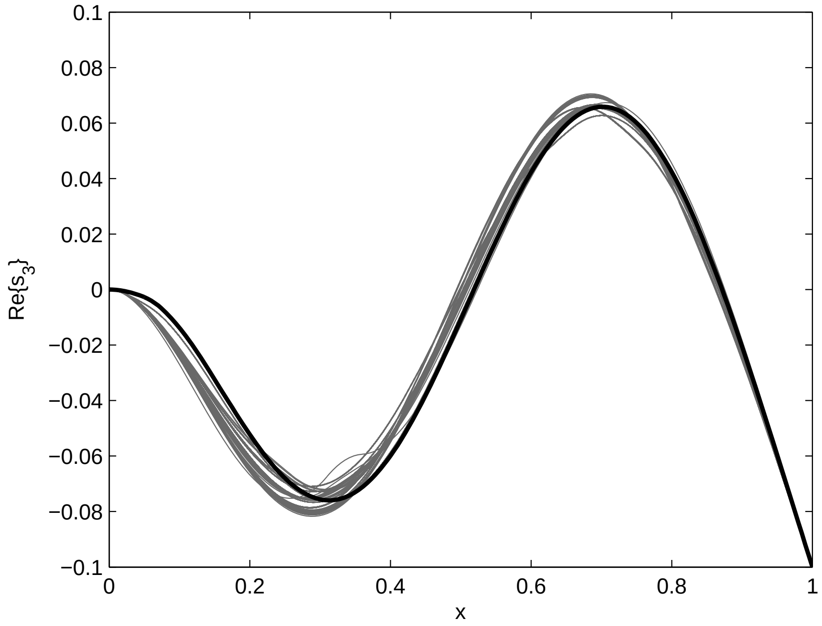

Figure 5.8: Envelope of the third modeshapes obtained at 12 PZT locations considered in this study, before saturation limit.

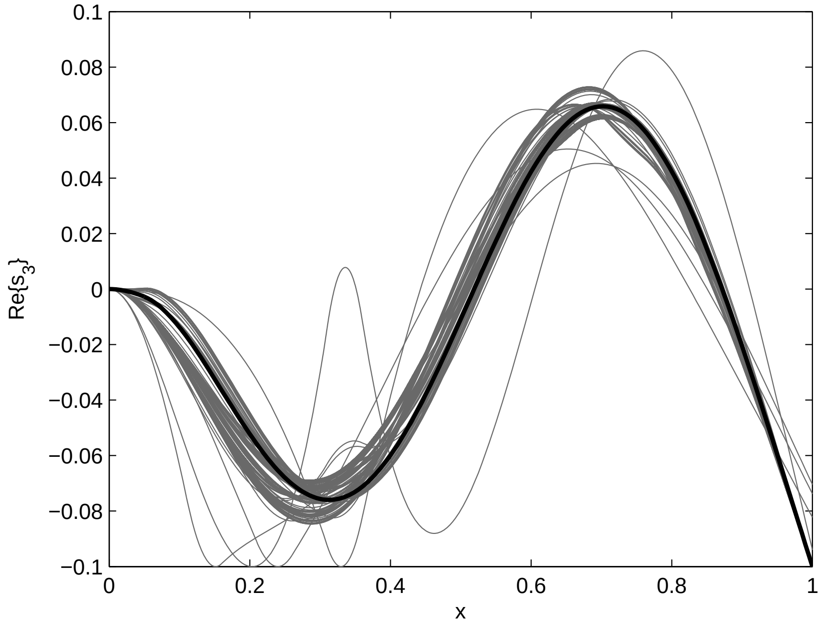

Figure 5.9: Envelope of the third modeshapes obtained at 12 PZT locations considered in this study, no saturation constraints considered.

5.4 Biomimetic Propulsion Comments

In terms of the potential for surface bonded PZT patches to assist biologically inspired propulsion systems, it is known that most fish generate thrust by bending their bodies into backward-moving propulsive waves that extend to its caudal fin. This is referred to as body and/or caudal Fin(BCF) locomotion [4]. The BCF locomotion can be classified into four subgroups, as shown earlier in Figure 1.5.

Comparing the BCF shapes in Figure 1.5 with first three mode shapes of the clamped-free beam, one can see that *thunniform* propulsion regime corresponds to the first mode, *subcarangiform* and *carangiform* regimes correspond to the second mode and *anguilliform* regime corresponds to the third mode. As was mentioned in Section 5.2, the mode shapes were normalized to ensure that the maximum deflection was $0.1L$. The choice of this particular value was based on tail beat amplitudes of $0.13L - 0.2L$ observed in shark, trout, tuna and goldfish [51], [52]. Also, the choice ensured that the vibration remained well within the realm of Euler-Bernoulli theory.

Each particular swimming movement has its own traits. The *anguilliform* swimming mode is recognized to be slower but the most efficient. Many anguilliform swimmers are capable of backward as well as forward swimming by altering the propagation direction of the propulsive wave [4]. On the other hand,*thunniform* is recognized to be the fastest. This locomotion mode evolved in the aquatic environment, where thrust is generated by the lift-based method, allowing high cruising speeds to be maintained for long periods. However, the design of *thunniform* swimmers is optimized for high-speed swimming in calm waters and is not well-suited to other actions such as slow swimming, turning maneuvers, and rapid acceleration from stationary and turbulent water (streams, tidal rips, etc.)[4].

It may be desirable for a vehicle employing fish type swimming to operate in different regimes, depending whether it needs to move faster or to conserve energy. Based on the observations of Long [1], the ability to actively modulate the natural modes of a flexible propulsor to match a changing tailbeat frequency should make it possible to improve efficiency. From Figures 5.3 – 5.4 $Im\{s_2\}$ is in the range of $2.02 - 2.1$Hz, and $Im\{s_3\}$ is in the range of $5.3 - 5.8$Hz. The BCF group of fish exhibit tailbeat frequencies in the range of 2.0Hz to 5.8Hz across all four regimes of BCF swimming. Hence, the single PZT patch, placed at the base of a caudal area, may afford a match between the natural frequency of the caudal fin and the oscillating frequency of the primary actuator. For this application, the caudal area of the tail has to be made very flexible in order to accept the PZT stiffening effect seen in Figures 5.2, 5.3 and 5.4 without increasing frequency too high. This appears to be more applicable for swimming vehicles that mimic the *anguilliform* and *subcarangiform* types of swimming, since the frequency adjustments possible in the second and third modes are greater then that attained for a first mode.

Presuming a vehicle is designed for a *thunniform mode*, A-type control, as is, can't make second or third modes descend into frequency range of swimming machine. Therefore, A-type control could be used to make a *thunniform mode* possible for a vehicle designed for *subcarangiform* and/or *anguilliform* swimming, but it is unlikely that a tail material could be found that attains a second or third mode in the $2.0 - 5.8$Hz frequency range expected.

Chapter 6

Conclusions

6.1 Summary

The are two main objectives of this thesis corresponding to the two topics considered. The first part of the thesis was dedicated to the comparison study of the caudal fin kinematics and mechanics. The caudal fin motion was represented by an oscillating plate propulsion system. The second part of the thesis consisted of modeling and numerical investigation on how PZTs could be used to assist various tail motions that drive the oscillating plate.

In the first part of the thesis, direct force measurements were used to conclude that a more elastic plate has better propulsion characteristics, namely thrust and efficiency, than the completely rigid one. By fixing the oscillating frequency at the values of Strouhal number that correspond to the maximum efficiency, the peak-to-peak amplitude of oscillation was varied in order to optimize the thrust and efficiency. It was concluded that Strouhal number, oscillating frequency and heave amplitude triplets such as $\{St = 0.3,\ f\ =\ 0.41Hz,\ \ h_0 = 16.1cm\}$, $\{St = 0.26, f = 0.36Hz, h_0 = 15.9cm\}$ and $\{St = 0.28, f = 0.29Hz, h_0 = 15.8cm\}$ for 1 : 6, 1 : 1 and 1 : 0 rigid-to-flexible ratio plates respectively, are the optimal values that allow oscillating plate propulsion system to operate in thrust producing regime with highest efficiency.

The set of experiments for a plate oscillating at different depth of the water channel test section showed that depth increase leads to the increase in propulsive characteristics of the plate. With respect to experimental depth, the increase in thrust coefficient and efficiency was not homogeneous. In the region from free surface to middepth, the increase in the thrust coefficient was not significant. However, in the region from middepth to the floor of the test section of the water channel, the increase of the thrust coefficient was more profound. The special case when the plate was tangential to the undisturbed free surface showed that, for plates of all types of chordwise flexibility, there is a steep rise in thrust coefficient, whilst the efficiency asymptotically approaches its limit.

The impact of submergence depth on the efficiency was observed to be stronger with the increase of experimental depth. The unexpected high efficiency value that was observed near the channel floor is suggested to be due to ground effects on the oscillating plate.

A rapid decrease in propulsive efficiency after maximum was attained was observed in all experiments carried out. Possible ways to avoid this would be to change the cross section of the plate from simple rectangular to one of the NACA profiles and increase the plate aspect ratio. Free surface effects visualization combined together with PIV data analysis will help to determine the exact mechanism of interaction between free surface patterns generated by the propulsor and shed vorticity.

In the second part of the thesis, the eigenproblem formulation and the solution technique presented allow determination of the complex natural frequencies and associated modeshapes of transversely vibrating beams with a perfectly bonded PZT patch using A-type control. This technique allows continuous variation of the PZT actuator location and provides closed form expressions for the modeshapes. By executing the eigenproblem solution for a variety of PZT locations and feedback gains, it was shown that the mode shapes are sensitive to the PZT location and that the frequencies and shapes of the higher modes are very dependent on the actuator location and gain value.

The most effective PZT position was found to be the one located near the fixed end of a beam. In terms of potential application in biologically inspired propulsion systems, the single PZT patch, placed at the base of a caudal area, can be used to align the natural frequency of the caudal fin and the oscillating frequency of the primary actuator to improve efficiency. In addition to that, A-type control could be used to make a *thunniform mode* possible for a vehicle designed for *subcarangiform* and/or *anguilliform* swimming, however, for this application, the caudal area of the tail has to be made very flexible in order to accept the PZT stiffening effect.

In conclusion, the present approach provides a tool necessary for prediction and control design of surface bonded PZTs used to control the vibration of flexible cantilevered structures.

6.2 Recommendations for Future Work

The results presented in this thesis revealed a dependance of a harmonically oscillating plate propulsion system on the chordwise flexibility of the plate. However, the exact mechanism behind propulsion performance of an oscillating flexible plate and possible ways to improve it still needs to be addressed. For this purpose, it is suggested that the material presented in Chapter 3.5 should be expanded in a full scale flow visualization study. Preserving the same system configuration, the following technical improvements should be made.

The PIV system needs to be synchronized with the force measurement unit. The synchronization based on pitch angle value will allow effective phase averaging, a procedure that increases definition of vortical structures near the surface of the plate. The phase averaging also has its downside, it is based on the assumption that the flow is periodic with a known and constant period T. In this work, T is the plate motion period. Using the phase averaging method then amounts to determining an average velocity measurement point, which may be very different from the measured instantaneous velocity since certain peaks of the velocity signals may vanish, which in turn may cause the disappearance of certain vortical structures.

The PIV experiments for all cases reported in Chapter 3 will help to answer the following questions:

- How does leading edge separation affect the near surface and wake structure, and is there a noticeable dependance on plate chordwise flexibility and depth of submergence?
- Is there an increase in thrust and vortex strength with the increase of Strouhal number and possible angle of attack.
- Does phase angle influence the development of dynamic stall vortices and do they affect overall thrust generation. Is there a favorable placement of the dynamic stall vortices during an oscillation cycle and is there a way to control it?
- Is it possible to manipulate the stall process in order to increase efficiency?

By choosing plates of various thickness, it would be possible to investigate not only the effect of proximity of the plate's natural frequency to the frequency of oscillation, but also the influence of the oscillation frequency on the mode shapes of the plate.

This last part can be combined with an analytical study on PZT actuators location in order to determine the optimal placement of PZT patch for suppression of unnecessary vibration in the foil.

In terms of controlling the flexibility of the caudal area, it was shown that the saturation voltage limit present a real constraint for a single PZT patch. One of the possible ways to lessen that effect would be to consider an array of PZT patches. It should be noted that, by considering a conventional A-type control strategy, the PZT placement problem was considered from the vibration suppression point of view. For the biomimetic application considered here, it may be necessary to apply voltage to PZTs in such way that they induce moments in the direction opposite to the deformation. That is, when there is a goal to modify mode shapes, the PZTs should in fact create moments that act in the same direction as the deformation propagation. This will lead to negative values of the gain K_a. By taking $K_a < 0$ to increase flexibility, it might be possible that the *carangiform* mode can be lowered into the frequency range of a swimming machine, and be used for efficient cruising.

The modified transfer matrix technique that was used in this thesis for optimal single PZT patch placement selection should be extended to handle more complicated problems. As the use of a single PZT patch illustrated a good potential in frequency/mode shapes adjustment, it is natural to consider the action of several PZT patches on the mechanical characteristics of the EB cantilever beam. The addition of several PZT patches will obviously make the search/optimization procedure highly nonlinear and iterative. Besides that, the interelement conditions will need to be revisited, and the effect of PZT patch response on the action of neighboring PZT patches must be considered.

There is a hope that the series of experiments proposed above can be done in the near future and their outcome will reveal answers that can be used in different engineering applications.

Appendix A

Force distribution due to chordwise flexibility

Consider the two plates, rigid and flexible, are subject to identical oscillatory motion, as defined in Section 2.3, equations (2.1) and (2.2). Let U_∞ be the incoming flow velocity, $\Theta(t)$ the pitching angle, as shown in Figure A.1.

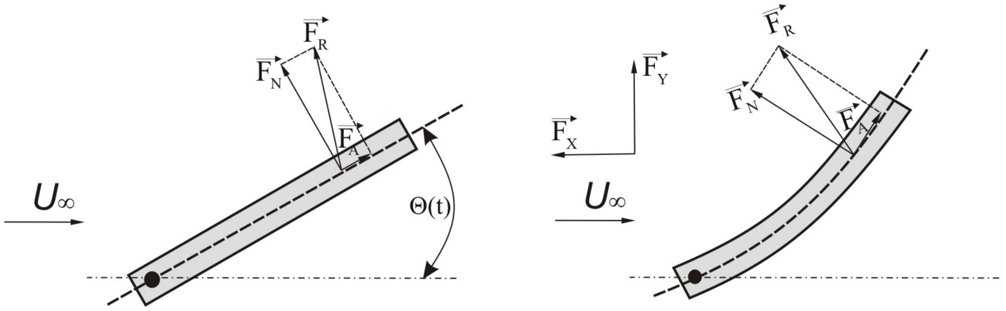

Figure A.1: Force distribution at the center of pressure of the rigid and flexible plates.

Under these conditions, every point of the upper and lower surface of each of the plates is subject to the normal and axial forces, $\vec{F}_N(t)$ and $\vec{F}_A(t)$ respectively. For the flexible plate, the plate's chord is distorted by the effect of hydrodynamic pressure which leads to the higher velocity near the curved part of the lower surface compared to the same section of the rigid plate. From Bernoulli's equation, higher velocity on the surface leads to the decrease in pressure there. Hence, one can see that the pressure distribution on the curved low surface of the flexible plate is lower then the pressure distribution on the same segment of the rigid plate.

Pressure is defined as a force per unit area, where by force, the normal force $\vec{F}_N(t)$

is assumed. Decrease in pressure on the lower surface of the flexible plate leads to the decrease in the magnitude of the resultant normal force over all low surface on that plate. So that, the magnitude of the resultant normal force on the low surface of the flexible plate is less the the magnitude of the resultant normal force on the rigid plate. As the instantaneous normal and axial forces $\vec{F}_N(t)$ and $\vec{F}_A(t)$ are measured by the load cell, it can be concluded that due to chordwise flexibility, the normal force on the flexible plate is lower then the normal force on the rigid plate for the same range of motion.

The transverse force $\vec{F}_y(t)$ is the projection of the force $\vec{F}_N(t)$ on the y-axis in laboratory coordinate frame, which was introduced in Section 3.1. Force $\vec{F}_y(t)$ is related to efficiency, by equation (3.5) through the average power defined by equation (3.2):

$$\eta_P = \frac{\bar{F}_x U}{\bar{P}}, \tag{A.1}$$

$$\bar{P} = \frac{1}{nT}\left(\int_0^{nT} F_y(t)\frac{dh}{dt}(t)dt + \int_0^{nT} M_z(t)\frac{d\theta}{dt}(t)dt\right), \tag{A.2}$$

As the transverse force $\vec{F}_y(t)$ is present in the denominator, its decrease leads to the increase in efficiency. Besides that, as shown in Figure A.1, the direction of the resultant force $\vec{F}_R(t)$ in in the direction of advance, which suggest the increase in thrust. This explains why the flexible plate operates at higher efficiency η_P than the rigid one.

Appendix B

Copyright permissions

Dear Oleksandr Barannyk,

I, Kevin Kelly - Boeing Trademarks & Copyrights, authorize you to include in your thesis/dissertation the Boeing 747 photo, ID #K63636-01, available on the www.boeing.com website. Your use falls within the Fair Use guidelines of US Copyright Law. Please include a credit of "(c) Boeing" for the image.

I am aware this is an irrevocable non-exclusive license allowing the Library and Archives Canada to reproduce, loan, distribute or sell copies of this thesis/dissertation by any means and in any form or format to make it available to interested persons. Approved sales of this work are limited to non-commercial use to cover the cost of reproducing the thesis/dissertation.

Sincerely,

Kevin S. Kelly Boeing Intellectual Property Management Trademark and Copyright Licensing

---

Dear Mr. Oleksandr Barannyk,

please use the picture of BASS-III for your thesis.

With best regards, Naomi Kato

Good morning Mr. Barannyk

IHC Engineering Business Ltd is more than happy for you to use this image. Please refer to the image as courtesy of IHC Engineering Business Ltd, if and when it is used.

Regards Vicky Mason PA/Sales and Marketing Assistant IHC Engineering Business Ltd

Bibliography

[1] J. H. Long and K. S. Nipper, “The importance of body stiffness in undulatory propulsion,” *American Zoologist*, vol. 36, pp. 678–694, 1996.

[2] M. E. Demont and J. M. Gosline, “Mechanics of jet propulsion in the hydromedusan jellyfish, polyorchis-penicillatus .1. mechanical-properties of the locomotor structure,” *Journal of Experimental Biology*, vol. 134, pp. 313–332, 1988.

[3] M. E. Demont, “Tuned oscillations in the swimming scallop pecten-maximus,” vol. 68, pp. 786–791, 1990.

[4] M. Sfakiotakis, D. M. Lane, and J. Davies, “Review of fish swimming modes for aquatic locomotion,” *Ieee Journal of Oceanic Engineering*, vol. 24, no. 2, pp. 237–252, 1999.

[5] K. V. Rozhdestvensky and V. A. Ryzhov, “Aerohydrodynamics of flapping-wing propulsors,” *Progress in Aerospace Sciences*, vol. 39, no. 8, pp. 585–633, 2003.

[6] N. Isshiki, H. Mirikawa, and H. Kato, “The study on a propulsion system by fin stroke.,” *Bulletin of Marine Engineering Society in Japan*, vol. 8, no. 1, pp. 71–79, 1980.

[7] K. A. Harper, M. D. Berkemeier, and S. Grace, “Modeling the dynamics of spring-driven oscillating-foil propulsion,” *IEEE Journal of Oceanic Engineering*, vol. 23, no. 3, pp. 285–296, 1998.

[8] J. E. Colgate and K. M. Lynch, “Mechanics and control of swimming: A review,” *IEEE Journal of Oceanic Engineering*, vol. 29, no. 3, pp. 660–673, 2004.

[9] N.Kato and M.Furushima, “Pectoral fin model for maneuver of underwater vehicles,” *Proceedings of the 1996 Symposium on Autonomous Underwater Vehicle Technology, AUV ’96*, 1996.

[10] N. Kato, W. Bugi, and Y. Suzuki, “Swimming performance of biology-inspired autonomous underwater vehicle “bass iii” with a pair of mechanical pectoral fins,” *Proc. of 1st International Symposium on Aqua Bio-Mechanisms*, pp. 315–320, 2000.

[11] S. Sunada, K. Kawachi, A. Matsumoto, and A. Sakaguchi, “Unsteady forces on a two-dimensional wing in plunging and pitching motions,” *Aiaa Journal*, vol. 39, no. 7, pp. 1230–1239, 2001.

[12] D. A. Read, F. S. Hover, and M. S. Triantafyllou, “Forces on oscillating foils for propulsion and maneuvering,” *Journal of Fluids and Structures*, vol. 17, no. 1, pp. 163–183, 2003.

[13] J. Lighthill, “Aquatic animal propulsion of high hydromechanical efficiency,” *Journal of Fluid Mechanics*, vol. 44, no. NOV11, p. 265, 1970.

[14] J. Lighthill, “Fundamentals concerning wave loading on offshore structures,” *Journal of Fluid Mechanics*, vol. 173, pp. 667–681, 1986.

[15] J. C. Lin and D. Rockwell, “Force identification by vorticity fields: Techniques based on flow imaging,” *Journal of Fluids and Structures*, vol. 10, no. 6, p. 663, 1996.

[16] F. Noca, D. Shiels, and D. Jeon, “A comparison of methods for evaluating time-dependent fluid dynamic forces on bodies, using only velocity fields and their derivatives,” *Journal of Fluids and Structures*, vol. 13, no. 5, pp. 551–578, 1999.

[17] J. O. Dabiri, “On the estimation of swimming and flying forces from wake measurements,” *Journal of Experimental Biology*, vol. 208, no. 18, pp. 3519–3532, 2005.

[18] J. Katz and D. Weihs, “Hydrodynamic propulsion by large-amplitude oscillation of an airfoil with chordwise flexibility,” *Journal of Fluid Mechanics*, vol. 88, pp. 485–497, 1978.

[19] J. Young, S. M. Walker, R. J. Bomphrey, G. K. Taylor, and A. L. R. Thomas, “Details of insect wing design and deformation enhance aerodynamic function and flight efficiency,” *SCIENCE*, vol. 325, no. 5947, pp. 1549–1552, 2009.

[20] K. Tatsuro, K. Hiroharu, K. Akihiro, and Y. Hajime, “Study on propulsion by partially elastic oscillating foil (1st report). analysis by linearized theory.,” *Journal of the Society of Naval Architects of Japan*, vol. 156, pp. 82–101, 1984.

[21] K. Tatsuro, K. Hiroharu, K. Akihiro, and Y. Hajime, “Study on propulsion by partially elastic oscillating foil (2nd report). numerical simulations by singularity distribution method and evaluation of scompe for application to ship propulsion.,” *Journal of the Society of Naval Architects of Japan*, vol. 156, pp. 92–101, 1984.

[22] J. Grue, A. Mo, and E. Palm, “Propulsion of a foil moving in water-waves,” *Journal of Fluid Mechanics*, vol. 186, pp. 393–417, 1988.

[23] Q. Zhu, Y. M. Liu, and D. K. P. Yue, “Dynamics of a three-dimensional oscillating foil near the free surface,” *AIAA Journal*, vol. 44, pp. 2997–3009, 2006.

[24] C. Lindsey, *“Form, function and locomotory habits in fish”, in Fish Physiology Vol. VII Locomotion, W.S.Hoar and D.J. Randall, Eds.* New York: Academic Press, 2003.

[25] D. Sun, J. K. Mills, J. J. Shan, and S. K. Tso, “A PZT actuator control of a single-link flexible manipulator based on linear velocity feedback and actuator placement,” *Mechatronics*, vol. 14, no. 4, pp. 381–401, 2004.

[26] K. Gurses, B. J. Buckham, and E. J. Park, “Vibration control of a single-link flexible manipulator using an array of fiber optic curvature sensors and PZT actuators,” *Mechatronics*, vol. 19, no. 2, pp. 167–177, 2009.

[27] T. P. Chang, F. I. Chang, and M. F. Liu, “On the eigenvalues of a viscously damped simple beam carrying point masses and springs,” *Journal of Sound and Vibration*, vol. 240, no. 4, pp. 769–778, 2001.

[28] J. M. Sloss, J. C. Bruch, I. S. Sadek, and S. Adali, “Integral equation approach for beams with multi-patch piezo sensors and actuators,” *Journal of Vibration and Control*, vol. 8, no. 4, pp. 503–526, 2002.

[29] A. Nashif, D. Jones, and J. Henderson, *Vibration Damping.* John Wiley & Sons, 1985.

[30] S. Sorrentino, S. Marchesiello, and B. A. D. Piombo, "A new analytical technique for vibration analysis of non-proportionally damped beams," *Journal of Sound and Vibration*, vol. 265, no. 4, pp. 765–782, 2003.

[31] E. F. Crawley and J. Deluis, "Use of piezoelectric actuators as elements of intelligent structures," *AIAA Journal*, vol. 25, no. 10, pp. 1373–1385, 1987.

[32] R. W. A.M. Sadri and J. Wright, "The design and implementation of robust strstegies for active vibration control," *In Proc. of the American control Conference*, pp. 3465–3469, 1998.

[33] S. Devasia, M. T., B. Paden, and E. Bayo, "Piezo-electric actuator design for vibration suppression: placement and sizing," *Proc. of the 31st Conference on Decision & Control*, pp. 1367–1372, 1992.

[34] S. Moheimani and T. Ryall, "Considerations on placement of piezoceramic actuators that are used in structural vibration control," *Proc. of the 38th Conference on Decision & Control*, pp. 1187–1193, 1999.

[35] J. M. Anderson, K. Streitlien, D. S. Barrett, and M. S. Triantafyllou, "Oscillating foils of high propulsive efficiency," *Journal of Fluid Mechanics*, vol. 360, pp. 41–72, 1998.

[36] G. D'antona and A. Ferrero, *Digital Signal Processing for Measuring Systems. Theory and Applications.* Springer, 2006.

[37] L. Levesque, "Simple smoothing technique to reduce data scattering in physics experiments," *European Journal of Physics*, vol. 29, no. 1, pp. 155–162, 2008.

[38] G. S. Triantafyllou, M. S. Triantafyllou, and M. A. Grosenbaugh, "Optimal thrust development in oscillating foils with application to fish propulsion," *Journal of Fluids and Structures*, vol. 7, no. 2, pp. 205–224, 1993.

[39] L. Schouveiler, F. S. Hover, and M. S. Triantafyllou, "Performance of flapping foil propulsion," *Journal of Fluids and Structures*, vol. 20, no. 7, pp. 949–959, 2005.

[40] M. M. Koochesfahani, "Vortical patterns in the wake of an oscillating airfoil," *Aiaa Journal*, vol. 27, no. 9, pp. 1200–1205, 1989.

[41] I. Yamamoto, Y. Terada, T. Nagamatu, and Y. Imaizumi, "Propulsion system with flexible rigid oscillating fin," *IEEE Journal of Oceanic Engineering*, vol. 20, no. 1, pp. 23–30, 1995.

[42] K. Isogai, Y. Shinmoto, and Y. Watanabe, "Effects of dynamic stall on propulsive efficiency and thrust of flapping airfoil," *AIAA Journal*, vol. 37, no. 10, pp. 1145–1151, 1999.

[43] Y. Tanida, "Ground effect in flight - (birds, fishes and high-speed vehicle)," *JSME International Journal Series B-Fluids and Thermal Engineering*, vol. 44, no. 4, pp. 481–486, 2001.

[44] J. H. J. Buchholz and A. J. Smits, "The wake structure and thrust performance of a rigid low-aspect-ratio pitching panel," *Journal of Fluid Mechanics*, vol. 603, pp. 331–365, May 25 2008.

[45] P. Freymuth, "Thrust generation by an airfoil in hover modes," *Experiments in Fluids*, vol. 9, no. 1-2, pp. 17–24, 1990.

[46] A. Thomas, G. Taylor, R. Srygley, R. Nudds, and R. Bomphrey, "Dragonfly flight: free-flight and tethered flow visualizations," *Journal of Experimental Biology*, vol. 207, pp. 4299–4323, NOV 2004.

[47] J. M. Anderson, *Vorticity control for efficient propulsion.* PhD Thesis, Massachusetts Institute of Technology, 1996.

[48] J. Ortega and W. Rheinboldt, *Iterative solution of nonlinear equations in several variables (Classics in Applied Mathematics, 30).* SIAM, 2000.

[49] S. Rao, *Mechanical Vibration (4th Edition).* Prentice Hall, 2003.

[50] D. Sun and J. K. Milles, "Study on piezoelectric actuators in control of a single-link flexible manipulator," *Proc. IEEE Int. Conf. on Robotics and Automation (Detroit, MI) (Piscataway, NJ: IEEE)*, vol. 2, pp. 849–854, 1999.

[51] H. Dewar and J. Graham, "Studies of tropical tuna swimming performance in a large water tunnel – energetics," *J Exp Biol*, vol. 192, no. 1, pp. 13–31, 1994.

[52] F. R. Harden Jones, "Tail beat frequency, amplitude, and swimming speed of a shark tracked by sector scanning sonar," *ICES J. Mar. Sci.*, vol. 35, no. 1, pp. 95–97, 1973.